Journal of Heat and Mass Transfer Research

Journal homepage: https://jhmtr.semnan.ac.ir

Semnan University

ISSN: 2383-3068

Research Article

Impact of Hall and Ion Slip Conditions in Two Layered Peristaltic Flow of Casson-Micropolar and Newtonian Liquid in an Inclined Channel

Suripeddi Srinivas, J. Bala Anasuya *

Department of Mathematics, VIT-AP University, Inavolu, Amaravath, 522237, India

ARTICLE INFO

Article history:

Received: 2025-03-09

Revised: 2025-04-18

Accepted: 2025-05-23

Keywords:

Casson-Micropolar fluid;

Peristaltic transport;

Hall and ion slip;

Froude number;

Mechanical efficiency.

ABSTRACT

The study explores the impact of Hall and ion slip and velocity slip on the heat and mass transfer characteristics of MHD two-layered peristaltic motion of Casson-micropolar and Newtonian liquid in an inclined channel embedded in a porous space. The governing flow equations have been linearised under the assumptions of long-wavelength approximation and low Reynolds number. Closed-form expressions for pressure rise, wall frictional force, and mechanical efficiency over a complete wavelength cycle are derived. Results are presented graphically to analyse the impact of key parameters, such as the Hartmann number, porous parameter, Froude number, velocity slip, and inclination parameter, on velocity, temperature, concentration, mechanical efficiency, entropy generation, along with Nusselt number and Sherwood number. Our findings reveal that as inclination, microrotation, and Casson parameters grow, there is a corresponding rise in liquid velocity. The liquid temperature falls with the rise of the Froude number and Casson parameter. Furthermore, when the chemical reaction parameter and Schmidt number grow, the concentration distribution reduces. It is also observed that when the micropolar fluid and inclination parameters rise, both the pressure gradient and pressure rise increases. Mechanical efficiency improves with the rise of the microrotation parameter, and entropy generation escalates with the rise in the inclination parameter. A comparative analysis has been performed to confirm the validity of the obtained results. These studies can be applied to physiological systems; specifically, esophageal peristalsis is governed by central and peripheral neural mechanisms, which involve extrinsic sympathetic or parasympathetic nerves and the myenteric plexus, respectively. Additionally, such investigations are relevant to biomedical engineering applications, including thermal therapy procedures.

1. Introduction

A progressive wave that contracts or expands along the length of a distensible tube or channel carrying the liquid is known as peristaltic transport. It is the main mechanism governing the flow of chyme and food in the intestines, the movement of spermatozoa through the cervical canal, the flow of bile in the bile ducts, and the passage of urine in the ureter. Finger and roller pumps use peristalsis to pump corrosive materials, preventing the fluid from touching the interior surfaces directly. The study of peristalsis has been receiving a lot of attention ever since the initial analysis carried out by Latham [1], both theoretical, computational and experimental studies have been extensively carried out to improve the understanding of peristaltic motion in various environments, due to its significance in

* **Corresponding author.**
E-mail address: bala2043@gmail.com

Cite this article as:
Srinivas, S. and Anasuya, J.B., 2025. Impact of Hall and Ion Slip Conditions in Two Layered Peristaltic Flow of Casson-Micropolar and Newtonian Liquid in an Inclined Channel. *Journal of Heat and Mass Transfer Research*, 12(2), pp. 345-376.
https://doi.org/10.22075/JHMTR.2025.37064.1690

biological systems and mechanical and industrial problems ([2]-[16] and several references therein).

In physiological systems like the ureter, esophagus, and small blood vessels, where the wall structure is responsible for pumping, the wall is often lined with a liquid that has different properties from the transported fluid. To understand the impact of this fluid coating on transport, it is necessary to expand the analysis of peristaltic pumping from a single fluid to a two-fluid model. This can be accomplished by introducing a peripheral layer with varying viscosity. Following Shukla et al. [17], researchers have shown a keen interest in this area of study [18-29]. The two fluid flow of a power-law fluid varying viscosities through a cylindrical tube has been analytically studied by Misra and Pandey [20]. Assuming a long wavelength and low Reynolds number, Kavitha et al. [21] examined the peristaltic motion of a Jeffrey liquid interacting with a Newtonian liquid in an inclined, symmetric channel. The peripheral region becomes narrower and the interface shape changes as the Jeffrey liquid parameter rises. The study by Vajravelu et al. [22] focused on the impact of peristalsis and heat transfer on physiological flow within a two-liquid model in a symmetric channel with permeable walls. The core contains a Jeffrey liquid and the periphery a Newtonian liquid. In a flexible cylindrical tube, Sadaqut Hussain et al. [23] have conducted an analysis of the two immiscible peristaltic pumping of Phan-Thien-Tanner liquid with applied electro-osmotic force. The fluid in the core (inner) layer follows the PTT fluid model's constitutive equation, whereas the fluid in the peripheral (outer) layer is Newtonian. The findings indicate that controlling trapping and reflux is possible through either increasing the electric field strength or leveraging the viscoelastic and extensional behavior of the fluid in the core region. Ali et al. [24] illustrated the peristaltic motion of two immiscible liquids in a tube along with electro-osmosis. At the periphery, fluid aligns with a Newtonian model, while the core fluid is represented by the Ellis constitutive equation. The streamline pattern is generated for each region when the interface's shape is not known beforehand. The flow and heat transfer characteristics of the peristaltic flow of two immiscible liquids in a vertical channel have been examined by Sankranthiand Akkiraju Naga Satya [25]. According to their results, an increase in viscosity ratio alters the interface shape, which leads to a reduced thickness of the peripheral layer in the pump's constricted region. Both zones are filled with Newtonian fluids with varying viscosity and density. Rushi Kesava and Srinivas [26] conducted an investigation on the peristaltic motion of a two-layered channel, with a Casson liquid in the inner layer and a porous space in the outer layer, considering a shear stress jump boundary condition at the interface. Sreenadh et al. [27] reported the influence of elasticity on the peristaltic transport of a Jeffrey and Newtonian liquid in a uniform tube using a two-layer liquid model. The results indicate that the elasticity of the tube walls causes the interface to extend more in the core region. Recently, Kumar and Yadav [28] explored heat and mass transfer characteristics in the peristaltic transport of immiscible Newtonian and micropolar liquid via a porous saturated channel along with the generation of entropy. The findings from the analysis highlight that naturally occurring porous materials lead to higher values of flow properties than man-made porous materials.

Non-Newtonian fluids have been a significant area of research for several decades. Due to the widespread use of various non-Newtonian fluids, such as lubricants, in industrial applications, considerable attention has been directed toward modelling and analysing their rheological properties. This non-linearity can appear in numerous fields, including food processing, drilling operations, and bioengineering (see the references [29-40]). The Casson micropolar fluid model combines the properties of Casson fluids, with their nonzero yield stress, and micropolar fluids, which exhibit micro-rotational behavior. This combination is vital in medical applications, particularly for blood rheology and the study of conditions like clotting or abnormal flow. Beyond medicine, the model is also valuable in predicting and controlling the flow of industrial fluids with complex compositions, such as slurries, emulsions, inks, and paints, which exhibit both viscoplastic and micropolar characteristics. Its accuracy is essential in fields that demand precise flow control, including biomedical devices, drug delivery systems, and microfluidic applications. Mehmood et al. [31] examined the effects of microrotation on the mixed convective flow of a Casson fluid driven by a stretched sheet. In their research, the velocity and microrotation profiles show opposing behaviour with respect to the micropolar parameter. Iqbal et al. [32] investigated the effects of an angled magnetic field and viscous dissipation on the flow of a micropolar Casson fluid across a stretched sheet. Using the scaling group of transformation the resulting system of equations are converted to a set of non-linear ODEs. These equations are then solved using the Keller box technique. The micropolar Casson fluid and its significant effects on the magnetic field were studied by Chun et al. [33]. The numerical procedure was carried out by use of the Lobatto IIIA numerical computing technique. The effects of material behavior, thermophoresis, the buoyancy ratio parameter, and Brownian motion, on MHD micropolar Casson liquid over a solid sphere enclosed by a porous space have been explored by Hazarika and Ahmed [34]. El-Dabe et al. [35] explored an incompressible micropolar Casson

fluid on a stretched surface with the influence of porous media and heat production. Ms-DTM has been employed to solve the governing equations. Abbas and Rafiq [36] analysed a numerical study on the peristaltic motion of micropolar-Casson liquid in a channel. Results indicated that a rise in the slip parameter, coupling number, and micropolar parameter leads to a reduction in the pressure gradient. The flow and thermal characteristics of a hybrid nanofluid Casson micropolar liquid over a curved stretching sheet was investigated by Upadhya et al. [37], along with mass transfer. In their results, the micropolar fluid exhibits more entropy generation than the Casson fluid. Nadeem Abbas et al. [38] explored the dynamic behaviour of Casson-Micropolar-Sutterby liquid flow over a sheet exhibiting exponential curvature, analysing the effects of chemical reactions and magnetic fields on the flow. Their results showed that the micropolar fluid profile curves increased with an increase in the curvature parameter values. Sharma et al. [39] employed computational techniques to investigate the thermal efficiency of immiscible Casson micropolar and Jeffery fluid flow in a horizontal channel with a uniform pressure gradient. Vaidehi and Sasikumar [40] examined the heat and mass transfer characteristics of micropolar-Casson liquid flow through a tapered oscillatory wavy channel, considering both low and high values of plastic dynamic viscosity. Where the radiation component of energy transfer is modelled using Plank's approximation. The Crank-Nicolson method is employed to resolve the governing equations.

In the presence of strong electromagnetic forces, the Hall effect becomes significant, especially when the Hall current is high due to a low electron-atom collision rate. Since ions possess greater mass than electrons, their movement differs, producing distinct diffusion velocities. Because current density depends on diffusion velocity, electrons typically contribute more to current flow than ions. However, under strong magnetic fields, ion diffusion becomes notable, and the combined influence of both ion and electron diffusion is known as the ion-slip effect. Both Hall and ion-slip effects are widely used in engineering applications such as Hall sensors, accelerators, and in the design of pumps and turbines. Recent relevant studies on this topic can be found in references [41-44].

Inspired by previous research, the focus is on studying the influence of Hall and ion slip along with velocity slip on the two immiscible peristaltic transport in an inclined channel through porous space along with heat and mass transfer characteristics. Such an investigation have not yet been reported in the literature. Moreover, the vasomotion of blood vessels, sperm transport in the male reproductive tract, movement through the cervical canal, oesophagus, and intestinal flow all involve a mucus layer lining the inner surface. In most of these vessels, fluid viscosity differs between the core and peripheral regions. Additionally, many organs are structured with core and peripheral zones, key to the thermal exchange between blood and tissue. Therefore, the proposed model can help facilitate this heat exchange process. This study investigates visco-plastic fluids that exhibit micro-rotation at the particle level where, Casson-micropolar liquid occupies the core region, whereas Newtonian fluid occupies the peripheral region. The Casson fluid model is applied to predict the flow nature of blood in arteries under low shear rates and accounts for non-zero yield stress, as well as understanding the behavior of pigment oil suspensions in printing inks, along with a dilute suspension of rigid, cylindrical, small macromolecules that move independently. Under the assumptions of long wavelength approximation and small Reynolds number, the conversion equations are linearised and solved. Closed-form expressions are provided for pressure rise, time-averaged flux, and Mechanical efficiency. The impact of pertinent parameters on flow, heat, mass distribution, mechanical efficiency, entropy generation, rate of heat transfer, and Sherwood number have been examined and presented graphically.

2. Flow Geometry

Consider peristaltic motion in a channel containing a Casson-micropolar and Newtonian liquid in the core and peripheral regions, respectively, see the Figure 1.

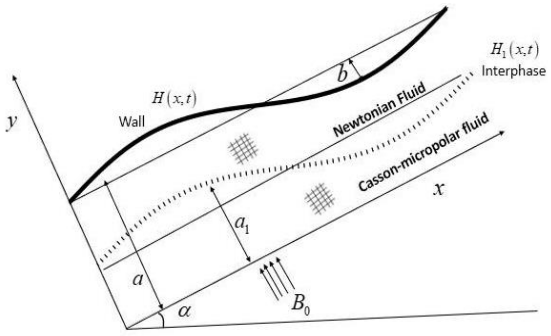

Fig. 1. Sketch of the model

3. Mathematical Formulation

The fluid flow within the channel where the walls are characterised by a time-varying function $H\left(\bar{X},t\right)=a+b\sin\frac{2\pi}{\lambda}\left(\bar{X}-ct\right)$ with the interface $H_1\left(\bar{X},t\right)=a_1+b_1\sin\frac{2\pi}{\lambda}\left(\bar{X}-ct\right)$ where b, b_1 are the amplitude, λ wavelength, c constant velocity with channel width a and a_1 is the width of the interface.

The mathematical formulation has been proceeded with the following assumptions,

- This study examines the peristaltic transport of two immiscible incompressible fluids in a symmetric porous channel.
- Wall deformation arises from the propagation of an infinite train of sinusoidal peristaltic waves defined by $y = h(x)$.
- The channel is inclined at an angle α with respect to the horizontal axis.
- The channel, whose length is considered an integral multiple of the peristaltic wavelength, is partitioned into two regions: a peripheral region occupied by a Newtonian fluid and a core region filled with a Casson micropolar fluid.
- A uniform pressure difference is applied across the channel boundaries, with a periodic interface condition.
- A uniform transverse magnetic field is imposed perpendicularly to the direction of fluid flow.
- The generalised Ohm's law is considered by accounting Hall and ion slip currents while neglecting thermoelectric effects.
- Two constant different temperatures T_1 and T_2 are maintained at the lower and upper walls of the channel.
- The analytical solution is determined under the assumptions of a long-wavelength approximation and a small Reynolds number.

The fundamental equations required to describe the flow problem are ([28], [32], [36])

$$\nabla \bar{U}_1 = 0$$

$$\rho_1\left(\frac{\partial \bar{U}_1}{\partial t} + \bar{U}_1.\nabla \bar{U}_1\right) = k\,(\nabla \times \bar{w}) + J \times B$$

$$+\mu_1\left(1 + \frac{1}{\beta} + k\right)\left(\nabla^2 \bar{U}_1\right) - \frac{\left(\frac{\mu_1}{\beta} + \mu_1 + k\right)}{K}\bar{U}_1$$

$$\rho_1 j\,(\bar{U}_1.\nabla)\bar{w} = k\,(\nabla \times \bar{U}_1) - 2k\bar{w} - \gamma\left(\nabla^2 \bar{w}\right) \tag{1}$$

$$\rho_1 c_p\left(\frac{\partial \bar{T}_1}{\partial t} + \bar{U}_1.\nabla \bar{T}_1\right) = \kappa_1 \nabla^2 \bar{T}_1 + \frac{1}{\sigma}(J \bullet J)$$

$$+\Omega_1 + Q_1 - \nabla q_{r_1} + b\left(\nabla w\,(\nabla w)^T\right)$$

$$+k\left(\frac{1}{2}\nabla \times \bar{U}_1 - w\right)$$

$$\left(\frac{\partial \bar{C}_1}{\partial t} + \bar{U}_1.\nabla \bar{C}_1\right) = D_1 \nabla^2 \bar{C}_1 + \frac{D_1 K_1}{T}\nabla^2 \bar{T}_1$$

$$-K_1\left(\bar{C}_1 - C_{w1}\right)$$

$$\nabla \bar{U}_2 = 0$$

$$\rho_2\left(\frac{\partial \bar{U}_2}{\partial t} + \bar{U}_2.\nabla \bar{U}_2\right) = \mu_2\left(\nabla^2 \bar{U}_2\right) + J \times B - \frac{\mu_2}{k}\bar{U}_2$$

$$\rho c_p\left(\frac{\partial \bar{T}_2}{\partial t}\bar{U}_2.\nabla \bar{T}_2\right) = \kappa_2 \nabla^2 \bar{T}_2 + \frac{1}{\sigma}(J \times J) + \Omega_2 + Q_2 - \nabla q_r \tag{2}$$

$$\left(\frac{\partial \bar{C}_2}{\partial t}\bar{U}_2.\nabla \bar{C}_2\right) = D_2 \nabla \bar{C}_2 + \frac{D_2 K_1}{T}\nabla^2 \bar{T}_2$$

$$-K_2\left(\bar{C}_2 - C_{w_1}\right)$$

$J \times B$ is the Lorentz force vector, and $\frac{1}{\sigma}J \times J$ is the Joule heating term. With the inclusion of Hall and ion slip effect, the generalised Ohm's law is represented as [36]:

$$J = \sigma(U \times B) - \frac{\omega_0 t_0}{B_0}(J \times B) + \frac{\omega_0 t_0 n_1}{B_0^{\,2}}((J \times B) \times B) \tag{3}$$

Using The Maxwell equations

$$J \times B = -\frac{\sigma B_0^{\,2}}{\beta_0^{\,2} + n_1^{\,2}}\begin{pmatrix}(\beta_0 U - n_1 V)i\\ +(\beta_0 V + n_1 U)j\end{pmatrix} \tag{4}$$

$$J \bullet J = \frac{\sigma^2 B_0^{\,2}}{\beta_0^{\,2} + n_1^{\,2}}\left(U^2 + V^2\right)$$

$$x = X - ct, \quad y = Y, \tag{5}$$

$$u = U - c, \quad v = V$$

Using the transformations given in the eqn (5) the governing equations are reduced to:

Core region

$$\frac{\partial u_1}{\partial x} + \frac{\partial v_1}{\partial y} = 0, \tag{6}$$

$$\rho_1\left(\frac{\partial u_1}{\partial t} + u_1\frac{\partial u_1}{\partial x} + v_1\frac{\partial u_1}{\partial y}\right) = -\frac{\partial p_1}{\partial x}$$

$$+\left(\mu_1\left(\frac{1}{\beta} + 1\right) + k\right)\left(\frac{\partial^2 u_1}{\partial x^2} + \frac{\partial^2 u_1}{\partial y^2}\right)$$

$$+k\,\frac{\partial w}{\partial y} + \rho g \sin\alpha - \frac{\mu_1}{K}u_1 \tag{7}$$

$$\frac{\sigma B^2}{\left(1 + \beta_1 n_1\right)^2 + n_1^{\,2}}\left((1 + \beta_1 n_1)u_1 - n_1 v_1\right)$$

$$\rho_1\left(\frac{\partial v_1}{\partial t}+u_1\frac{\partial v_1}{\partial x}+v_1\frac{\partial v_1}{\partial y}\right)=-\frac{\partial p_1}{\partial y}$$
$$-\left(\frac{\mu_1}{\beta}+\mu_1+k\right)\left(\frac{\partial^2 v_1}{\partial x^2}+\frac{\partial^2 v_1}{\partial y^2}\right)$$
$$-k\frac{\partial w}{\partial x}-\rho g\cos\alpha-\frac{\mu_1}{K^*}v_1$$
$$-\frac{\sigma B^2}{\left(1+\beta_1 n_1\right)^2+n_1^2}\left(\left(1+\beta_1 n_1\right)v_1-n_1u_1\right) \quad (8)$$

$$\alpha J\left(\frac{\partial w}{\partial t}+u_1\frac{\partial w}{\partial x}+v_1\frac{\partial w}{\partial y}\right)=-2kw$$
$$+\gamma\left(\frac{\partial^2 w}{\partial x^2}+\frac{\partial^2 w}{\partial y^2}\right)+k\left(\frac{\partial v_1}{\partial x}-\frac{\partial u_1}{\partial y}\right) \quad (9)$$

$$\rho c_p\left(\frac{\partial T_1}{\partial t}+u_1\frac{\partial T_1}{\partial x}+v_1\frac{\partial T_1}{\partial y}\right)=$$
$$\kappa_1\left(\frac{\partial^2 T_1}{\partial x^2}+\frac{\partial^2 T_1}{\partial y^2}\right)-\frac{\partial q_{r_1}}{\partial y}+Q_1$$
$$+k\left(\left(\frac{\partial u_1}{\partial y}+\frac{\partial v_1}{\partial x}\right)^2+2w\right)$$
$$+b\left[\left(\frac{\partial w}{\partial y}\right)^2+\left(\frac{\partial w}{\partial x}\right)^2\right] \quad (10)$$
$$+\left(\frac{\mu_1}{\beta}+\mu_1+k\right)\left\{2\left[\left(\frac{\partial u_1}{\partial x}\right)^2+\left(\frac{\partial v_1}{\partial x}\right)^2\right]+\left(\frac{\partial u_1}{\partial y}+\frac{\partial v_1}{\partial x}\right)^2\right\}$$
$$+\frac{\sigma B^2}{\left(1+\beta_1 n_1\right)^2+n_1^2}\left(u_1^2+v_1^2\right)$$

$$\left(\frac{\partial C_1}{\partial t}+u_1\frac{\partial C_1}{\partial x}+v_1\frac{\partial C_1}{\partial y}\right)=D_1\left(\frac{\partial^2 C_1}{\partial x^2}+\frac{\partial^2 C_1}{\partial y^2}\right)$$
$$-K_1\left(C_1-C_{w_1}\right)+\frac{D_1K_1}{T}\left(\frac{\partial^2 T_1}{\partial x^2}+\frac{\partial^2 T_1}{\partial y^2}\right) \quad (11)$$

Peripheral region

$$\frac{\partial u_2}{\partial x}+\frac{\partial v_2}{\partial y}=0, \quad (12)$$

$$\rho_2\left(\frac{\partial u_2}{\partial t}+u_2\frac{\partial u_2}{\partial x}+v_2\frac{\partial u_2}{\partial y}\right)=-\frac{\partial p_2}{\partial x}$$
$$+\mu\left(\frac{\partial^2 u_2}{\partial x^2}+\frac{\partial^2 u_2}{\partial y^2}\right)-\frac{\mu_2}{k_0}u_2+\sigma g\sin\alpha \quad (13)$$
$$-\frac{\sigma B^2}{\left(1+\beta_1 n_1\right)^2+n_1^2}\left(\left(1+\beta_1 n_1\right)u_2-n_1v_2\right)$$

$$\rho_2\left(\frac{\partial v_2}{\partial t}+u_2\frac{\partial v_2}{\partial x}+v_2\frac{\partial v_2}{\partial y}\right)=-\frac{\partial p_2}{\partial y}$$
$$-\mu\left(\frac{\partial^2 v_2}{\partial x^2}+\frac{\partial^2 v_2}{\partial y^2}\right)-\frac{\mu_2}{k_0}v_2-\sigma g\cos\alpha \quad (14)$$
$$-\frac{\sigma B^2}{\left(1+\beta_1 n_1\right)^2+n_1^2}\left(\left(1+\beta_1 n_1\right)v_2-n_1u_2\right)$$

$$\rho_2 c_p\left(\frac{\partial T_2}{\partial t}+u_2\frac{\partial T_2}{\partial x}+v_2\frac{\partial T_2}{\partial y}\right)=$$
$$\kappa_2\left(\frac{\partial^2 T_2}{\partial x^2}+\frac{\partial^2 T_2}{\partial y^2}\right)-\frac{\partial q_{r_2}}{\partial y}+Q_2$$
$$+\mu_2\left\{2\left[\left(\frac{\partial u_2}{\partial x}\right)^2+\left(\frac{\partial v_2}{\partial x}\right)^2\right]+\left(\frac{\partial u_2}{\partial y}+\frac{\partial v_2}{\partial x}\right)^2\right\} \quad (15)$$
$$+\frac{\sigma B^2}{\left(1+\beta_1 n_1\right)^2+n_1^2}\left(u_2^2+v_2^2\right)$$

$$\left(\frac{\partial C_2}{\partial t}+u_2\frac{\partial C_2}{\partial x}+v_2\frac{\partial C_2}{\partial y}\right)=$$
$$D_2\left(\frac{\partial^2 C_2}{\partial x^2}+\frac{\partial^2 C_2}{\partial y^2}\right)+\frac{D_2K_t}{T}\left(\frac{\partial^2 T_2}{\partial y^2}+\frac{\partial^2 T_2}{\partial x^2}\right) \quad (16)$$
$$-K_2\left(C_2-C_{w_2}\right)$$

The nondimensional parameters are:

$$x=\frac{x}{\lambda}, y=\frac{y}{a}, t=\frac{tc}{\lambda}, p=\frac{pa^2}{\mu_i c\lambda}, u_i=\frac{u_i}{c},$$
$$v_i=\frac{v_i\lambda}{cd}, w=\frac{wd}{c}, e=\frac{b}{a}, e_1=\frac{b_1}{a_1}, \eta=\frac{a_1}{a},$$
$$h_i=\frac{H_i}{a}, Da=\frac{K^*}{a^2}, \mu=\frac{\mu_2}{\mu_1}, \rho=\frac{\rho_2}{\rho_1},$$
$$\theta=\frac{T-T_{w_1}}{T_{w_1}-T_{w_2}}, \kappa=\frac{\kappa_2}{\kappa_1}, \phi=\frac{C-C_{w_1}}{C_{w_1}-C_{w_2}},$$
$$D=\frac{D_2}{D_1}, K=\frac{K_2}{K_1}, M=\sqrt{\frac{\sigma}{\mu_i}}B_0a, \quad (17)$$
$$\mathrm{Pr}=\frac{\mu_1 c_p}{\kappa_1}, Br=EcPr, Sc=\frac{\mu_1}{\rho D},$$
$$Sr=\frac{DK_T\Delta T_p}{T_m\mu_1\Delta C}, b_1=\frac{b}{\mu_1 a^2},$$
$$L=\frac{Rg_1DC_{w_1}}{\kappa_1}, \delta=\frac{\Delta T}{T_{w_1}}, \quad \Lambda=\frac{\Delta C}{C_{w_1}},$$
$$Ec=\frac{c^2}{c_p\Delta T}, Fr=\frac{\mu c}{\rho g a^3},$$

The Darcy number Da measures the permeability of a porous medium. The viscosity, density, and thermal conductivity ratios μ, ρ, and κ describe material property contrasts. The Brinkman number (Br) is a dimensionless parameter that represents the ratio of heat generated by viscous dissipation to the heat transferred through molecular conduction.. Mass transport behavior is captured through the Schmidt number Sc, Soret number Sr. The magnetic field effect is represented by the Hartmann number M, buoyancy effects are indicated by the modified Froude number Fr, Collectively, these dimensionless variables provide a generalised framework to analyse the coupled effects of flow, heat, and mass transfer.

Under the long-wavelength approximation, neglecting the term containing a/λ, we obtain

$$-\frac{\partial p_1}{\partial x}+\frac{1}{Fr}\sin\alpha+\frac{N}{1-N}\frac{\partial w}{\partial y}+\left(\frac{1}{\beta}+\frac{1}{1-N}\right)\frac{\partial^2 u_1}{\partial y^2}-\left(\frac{M^2(1+\beta_1 n_1)}{(1+\beta_1 n_1)^2+n_1^2}+\frac{MC}{Da}\right)u_1=0 \tag{18}$$

$$-2w+\frac{2-N}{m^2}\frac{\partial^2 w}{\partial y^2}-\frac{\partial u_1}{\partial y}=0 \tag{19}$$

$$(1+Rd)\frac{\partial^2 T_1}{\partial y^2}+\Upsilon_1+Br\left[\left(\frac{\partial u_1}{\partial y}+2w\right)^2+b_1\left(\frac{\partial w}{\partial y}\right)^2+\frac{M^2}{(1+\beta_1 n_1)^2+n_1^2}u_1^2\right]=0 \tag{20}$$

$$\frac{1}{Sc}\frac{\partial^2\phi_1}{\partial y^2}+Sr\frac{\partial^2\theta_2}{\partial y^2}-\xi\phi_1=0 \tag{21}$$

$$-\frac{\partial p_2}{\partial x}+\frac{\partial^2 u_2}{\partial y^2}+\frac{1}{\mu F_r}\sin\alpha-\left(\frac{M^2(1+\beta_1 n_1)}{(1+\beta_1 n_1)^2+n_1^2}+\frac{1}{Da}\right)u_2=0 \tag{22}$$

$$\left(\frac{\kappa+Rd}{\mu}\right)\frac{\partial^2 T_2}{\partial y^2}+Br\left(\frac{\partial u_2}{\partial y}\right)^2+Br\left(\frac{M^2}{(1+\beta_1 n_1)^2+n_1^2}\right)u^2{}_2+\Upsilon_1=0 \tag{23}$$

$$\frac{D}{Sc}\frac{\partial^2\phi_2}{\partial y^2}+Sr\frac{\partial^2\theta_2}{\partial y^2}-K\xi\phi_2=0 \tag{24}$$

The interface between the peripheral and core regions is represented by $y=h_1(x)$. At the lower boundary $y=0$, a no-slip condition is applied, whereas the upper wavy boundary $y=h(x)$ is characterized by slip conditions. Along with the velocity distribution, both the walls of the channel are maintained at different constant temperatures and concentrations.

$$\left.\begin{aligned}&u_1=0,\quad w=0,\\&\theta_1=0,\quad \phi_1=0,\end{aligned}\right\}y=0$$
$$\left.\begin{aligned}&u_2=\beta_2\frac{\partial u_2}{\partial y},\\&\theta_2=1,\ \phi_2=1\end{aligned}\right\}y=h=1+e\cos(2\pi x), \tag{25}$$

Whereas at the interface, velocity, shear stress, convective heat transfer, thermal flux, mass transfer, and mass flux remain continuous. And also, the angular micro-rotational velocity at the interface is defined as:

$$\left.\begin{aligned}&\frac{\partial w}{\partial y}=0,\ u_1=u_2,\\&\theta_1=\theta_2,\ \phi_1=\phi_2\end{aligned}\right\}y=h_1=\eta+e_1\cos(2\pi x)$$
$$\left.\begin{aligned}&\left(\frac{1}{\beta}+\frac{1}{1-N}\right)\frac{\partial u_1}{\partial y}-\frac{N}{1-N}w=\mu\frac{\partial u_2}{\partial y}\\&\frac{\partial\theta_1}{\partial y}=\kappa\frac{\partial\theta_2}{\partial y},\\&\frac{\partial\phi_1}{\partial y}=D\frac{\partial\phi_2}{\partial y},\end{aligned}\right\}y=h_1 \tag{26}$$

The arbitrary constants in the solution of the equations (18) –(24) have been obtained using the above boundary conditions eqn 25 and 26 where, the solutions are given by

$$w(y)=g_1\cosh(a_1 y)+g_2\sinh(a_1 y)+g_3\cosh(a_2 y)+g_4\sinh(a_2 y) \tag{27}$$

$$u_1(y)=-\frac{H}{M_1}+N_6+N_9 g_2\cosh(a_1 y)+N_9 g_1\sinh(a_1 y)+N_{10}g_3\sinh(a_2 y)+N_{10}g_4\cosh(a_2 y) \tag{28}$$

$$u_2(y)=c_5\cosh(a_3 y)+c_6\sinh(a_3 y)-\frac{H}{a_3^2}+\frac{\sin\alpha}{Fr\,a_3^2} \tag{29}$$

$$\theta_1(y) = d_1 + yd_2 - \frac{1}{8(1+Rd)}(A_1 y^2 + A_2 \cosh(2a_1 y) + A_3 \cosh((a_1 - a_2)y) + A_4 \cosh(2a_2 y) + A_5 \cosh((a_1 + a_2)y) + A_6 \sinh(2a_1 y) + A_7 \sinh((a_1 - a_2)y) + A_8 \sinh(2a_2 y) + A_9 \sinh((a_1 + a_2)y) + A_{10} \cosh(a_1 y) + A_{11} \cosh(a_2 y) + A_{12} \sinh(a1y) + A_{13} \sinh(a2y)) \quad (30)$$

$$\theta_2(y) = d_3 + yd_4 - \frac{1}{4a_3 J(1+Rd)}\mu(A_{14} y^2 + A_{15} \cosh(2a_3 y) + A_{16} \sinh(2a_3 y) + A_{17} \sinh(2a_3 y) + A_{18} \cosh(a_3 y) + A_{19} \sinh(a_3 y)) \quad (31)$$

$$\phi_1(y) = e_1 \cosh(f_1 y) + e_2 \sinh(f_1 y) + A_{20} y - A_{21} \sinh(2a_1 y) + A_{22} \sinh((a_1 - a_2)y) - A_{23} \sinh(2a_2 y) + A_{24} \sinh((a_1 + a_2)y) - A_{25} \cosh(2a_1 y) + A_{26} \cosh((a_1 - a_2)y) - A_{27} \cosh(2a_2 y) + A_{28} \cosh((a_1 + a_2)y) - A_{29} \sinh(a_1 y) - A_{30} \sinh(a_2 y) - A_{31} \cosh(a_1 y) - A_{32} \cosh(a_2 y) + A_{33} \quad (32)$$

$$\phi_2(y) = e_3 \cosh(f_2 y) + e_4 \sinh(f_2 y) - A_{34} y - A_{35} \sinh(2a_3 y) - A_{36} \cosh(2a_3 y) - A_{38} \sinh(a_3 y) - A_{39} \cosh(a_3 y) + A_{40} \quad (33)$$

The dimensionless instantaneous flow rate is given by

$$q = \int_0^{h_1} u_1 dy + \int_{h_1}^{h} u_2 dy \quad (34)$$

The mass must be conserved independently in the core and peripheral areas, since the viscosity ratio influences the shape of the interface (Li and Brasseur, 1993). The assumption is made that the interface form is not affected by the viscosity ratio. Consequently, it is possible to utilise the fact that the overall flux is the sum of the fluxes across the different sections: $0 \le y \le h_1$ and $h_1 \le y \le h$.

Following the analysis of [14] the relationship between e_1 and h_1 is provided by [17].

$$e_1 = \eta e, \quad h_1 = \eta h \quad (35)$$

The pressure rise over one wavelength is

$$\Delta p = \int_0^1 \frac{\partial p}{\partial x} dx = \int_0^1 H\, dx \quad (36)$$

Over one wavelength, the mean volume flow is [18].

$$Q = q + 1 + \frac{e^2}{2} \quad (37)$$

The dimensionless friction force

$$F = \int_0^1 h\left(-\frac{\partial p}{\partial x}\right)dx = \int_0^1 h(-H)\,dx \quad (38)$$

Mechanical efficiency is defined as the ratio of the average rate at which the moving fluid performs work against a pressure head over each wavelength to the average rate at which the walls transfer work to the fluid and is given by

$$E = \frac{Q\,\Delta p}{e\left(\int_0^1 \frac{\partial p}{\partial x}\cos(2\pi x)dx - \Delta p\right)} \quad (39)$$

In any thermal system, entropy generation is unavoidable, leading to the degradation of the system's available energy

$$S_{g_1} = \frac{k_1}{T^2_{w_1}}\left(1 + \frac{16\sigma^* T^3_{w_1}}{3k^* k_1}\right)\left(\frac{\partial T_1}{\partial y}\right)^2 + \frac{b}{T_{w_1}}\left(\frac{\partial w}{\partial y}\right)^2 + \left(\frac{\mu_1}{\beta} + \mu_1 + k\right)\left(\frac{\partial u_1}{\partial y}\right)^2 + \frac{R_{g_1} D_1}{C_{w_1}}\left(\frac{\partial g_1}{\partial y}\right)^2 + \frac{R_{g_1} D_1}{T_{w_1}}\left(\frac{\partial g_1}{\partial y}\frac{\partial T_1}{\partial y}\right) \quad (40)$$

$$S_{M_2} = \frac{k_2}{T^2_{w_1}}\left(1 + \frac{16\sigma^* T^3_{w_1}}{3k^* k_1}\right)\left(\frac{\partial T_2}{\partial y}\right)^2 + \mu_2\left(\frac{\partial u_2}{\partial y}\right)^2 + \frac{R_{g_1} D_2}{C_{w_1}}\left(\frac{\partial g_2}{\partial y}\right)^2 + \frac{R_{g_1} D_2}{T_{w_1}}\left(\frac{\partial g_2}{\partial y}\frac{\partial T_2}{\partial y}\right) \quad (41)$$

In the eqn (40), the terms on the RHS denote entropy generation from heat flow, viscous dissipation of Casson-micropolar liquid, and the effect of the magnetic field, respectively.

The dimensionless entropy generation number, Eg, following [37] is the ratio of the volumetric entropy generation rate to the characteristic entropy generation rate. The non-dimensional representation of the generation of entropy for both regions are:

$$Eg_1 = (1+Rd)\left(\frac{\partial \theta_1}{\partial y}\right)^2 + L\left[\left(\frac{\delta}{\xi}\right)^2\left(\frac{\partial \phi_1}{\partial y}\right)^2 + \frac{\partial \phi_1}{\partial y}\frac{\partial \theta_1}{\partial y}\right] + \frac{Br}{\xi}\left[\left(\frac{\partial u_1}{\partial y}\right)^2 + \frac{M^2}{\left((1+\beta_1)^2+n_1^2\right)}u_1^2 + \frac{N}{1-N}\left(\frac{\partial u_1}{\partial y}+2w\right)+\Omega\left(\frac{\partial w}{\partial y}\right)^2\right] \quad (42)$$

$$Eg_2 = \left(1+\frac{Rd}{k}\right)\left(\frac{\partial \theta_2}{\partial y}\right)^2 + \frac{Br\,\mu}{k\,\xi}\left[\left(\frac{\partial u_1}{\partial y}\right)^2 + M^2 u_2^2\right] + \frac{LD}{k}\left[\left(\frac{\delta}{\xi}\right)^2\left(\frac{\partial \phi_2}{\partial y}\right)^2 + \frac{\partial \phi_2}{\partial y}\frac{\partial \theta_2}{\partial y}\right] \quad (43)$$

To assess the irreversibility distribution, the Bejan number (Be) is used and is given by:

$$Be_1 = \frac{(1+Rd)\left(\frac{\partial \theta_1}{\partial y}\right)^2 + L_1}{Eg_1}, \qquad L_1 = L\left[\left(\frac{\delta}{\xi}\right)^2\left(\frac{\partial \phi_1}{\partial y}\right)^2 + \frac{\partial \phi_1}{\partial y}\frac{\partial \theta_1}{\partial y}\right] \quad (44)$$

$$Be_2 = \frac{\left(1+\frac{Rd}{k}\right)\left(\frac{\partial \theta_2}{\partial y}\right)^2 + L_2}{Eg_2}, \qquad L_2 = \frac{LD}{k}\left[\left(\frac{\delta}{\xi}\right)^2\left(\frac{\partial \phi_2}{\partial y}\right)^2 + \frac{\partial \phi_2}{\partial y}\frac{\partial \theta_2}{\partial y}\right] \quad (45)$$

The Bejan number ranges between 0 to 1, where $Be = 0$ highlights that viscous dissipation is the dominant contributor to irreversibility, and $Be = 1$ points to the dominance of heat transfer in irreversibility. At $Be = 0.5$, the irreversibility resulting from heat transfer is the same as that from viscous dissipation in the entropy production.

The rate of heat transfer is given by

$$Nu_1 = \left.\frac{\partial \theta_1}{\partial y}\right|_{y=h_1}, \qquad Nu_2 = \left.\frac{\partial \theta_2}{\partial y}\right|_{y=h} \quad (46)$$

The rate of mass transfer is expressed as

$$Sh_1 = \left.\frac{\partial \phi_1}{\partial y}\right|_{y=h_1}, \qquad Sh_2 = \left.\frac{\partial \phi_2}{\partial y}\right|_{y=h_2} \quad (47)$$

4. Results and Discussion

The equations for flow, energy, and concentration have been solved after linearization by utilising a long-wavelength approximation and a low-Reynolds number. The effects of parameter variations on velocity, micro-rotation, temperature, and concentration, with a specific focus on Hall and ion slip influences, are demonstrated in Figure 2 to Figure 12.

One can observe that velocity is higher in the presence of Hall and ion slip effects compared to their absence. Mathematica's built-in command, NIntegration was employed to obtain values for the pressure rise, friction force over one wavelength, and mechanical efficiency. The findings are shown graphically by altering the relevant parameters in Figure 13 to Figure 16.

Figure 17 and Figure 18 depict both entropy generation and the Bejan number. Figure 19 and Figure 20 deal with variations in the Nusselt number and Sherwood number. The 3D plots for velocity, temperature, and concentration distributions, as well as mechanical efficiency, are presented, emphasising the influence of Hall and ion slip conditions.

With the rise of M, the velocity and temperature distributions reduce, as depicted in Figure 2(a) and Figure 2(b). The presence of a transverse magnetic field generates a Lorentz force that acts as a drag force, opposing the flow and thereby diminishing both the fluid's velocity and temperature distribution. Figure 2(c) shows that microrotation intensifies with an increase in M.

Figure 3(a) and Figure 3(b) reveal that an increase in the permeability parameter Da is found to enhance the velocity distribution, primarily due to the absence of porous material that typically restricts fluid and temperature flow. It is evident from Figure 3(c) that microrotation exhibits a reverse pattern.

Figure 4(a) and Figure 4(b) indicate that as the channel's inclination angle, $\sin\alpha$, increases, the velocity and temperature of the fluid also rise, due to the strengthening effect of gravity with greater inclination angles. Conversely, Figure 4(c) shows that microrotation decreases as $\sin\alpha$ increases.

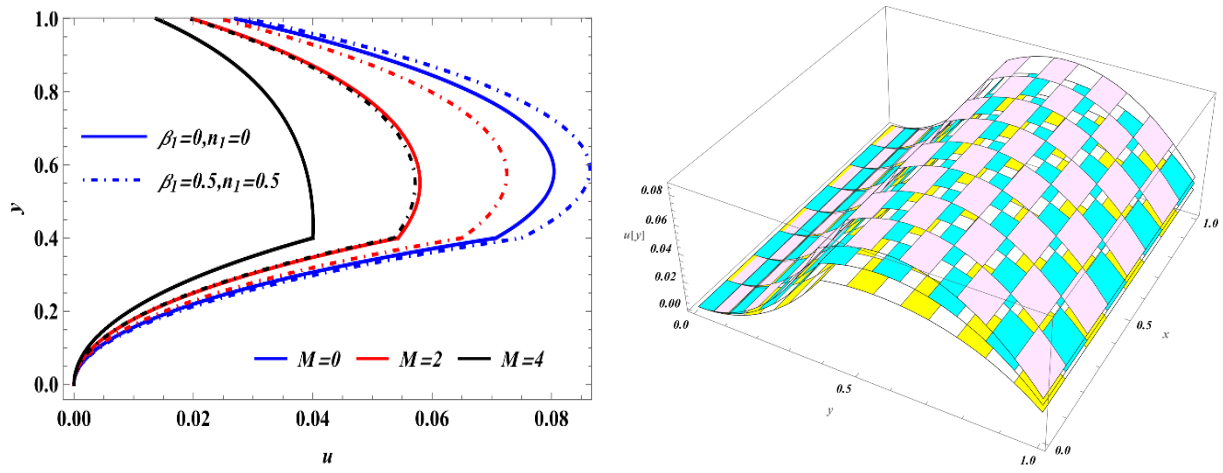

(a)

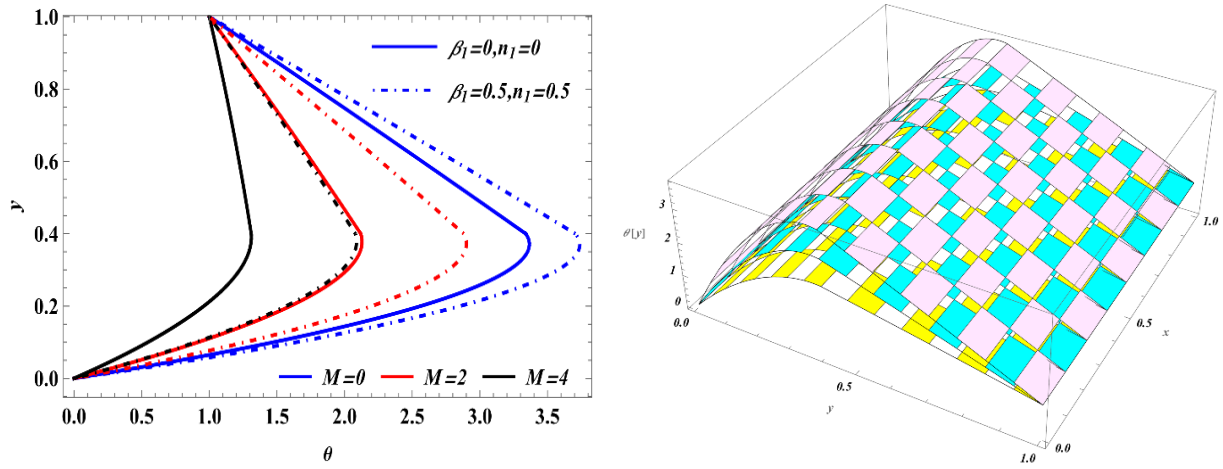

(b)

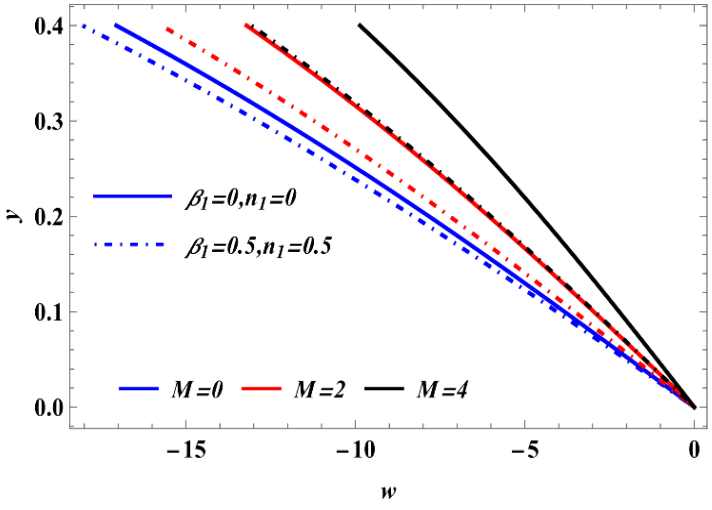

(c)

Fig. 2. Variations of a) Velocity; b) Temprature ; c) Microrotation velocity with M for $Fr = 0.2, sin\alpha = 0.1$, $Da = 0.5, \mu = 0.5, \varepsilon = 0.5, \varepsilon_1 = 0.6, \beta$=0.4, N=0.2, m=2, a=1, a_1=0.4, Rd=1, Q=1, k=0.5

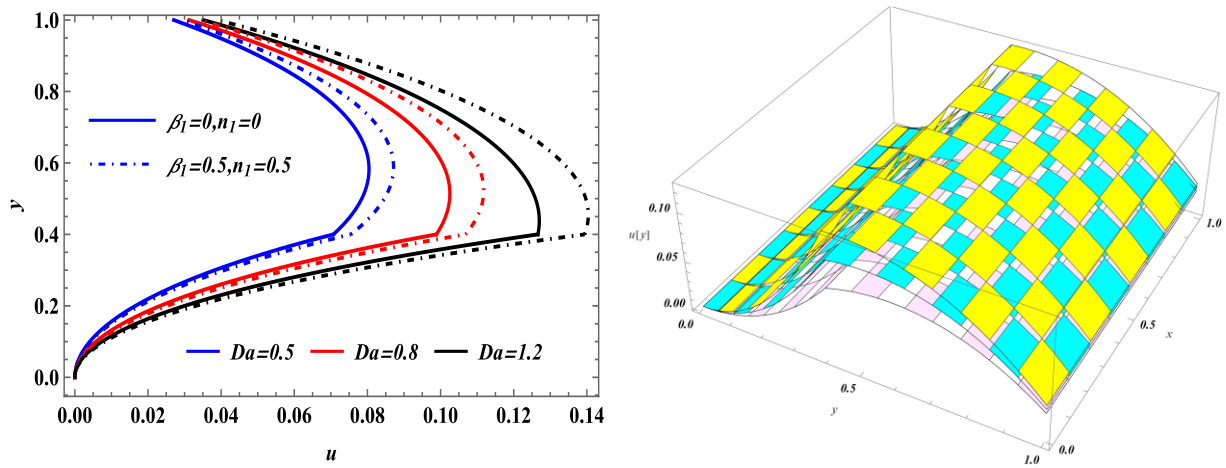

(a)

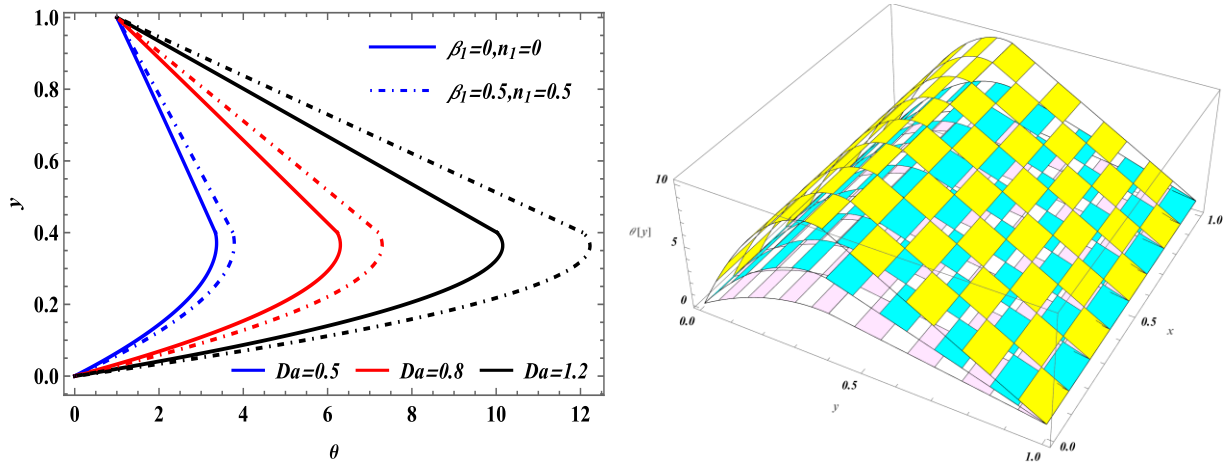

(b)

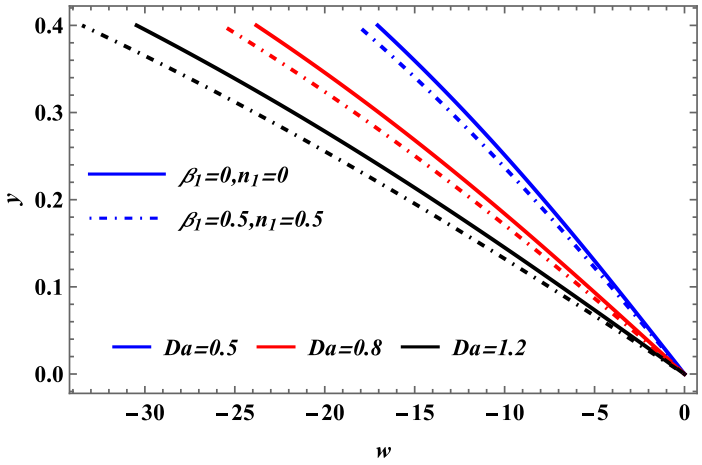

(c)

Fig. 3. Variations of a) Velocity; b) Temprature ; c) Microrotation velocity with *Da* for $Fr = 0.2, sin\alpha = 0.1$, $\mu = 0.5, \varepsilon_1 = 0.6, \beta$=0.4, *N*=0.2, *m*=2, *a*=1, a_1=0.4, *Rd*=1, *Q*=1, *k*=0.5

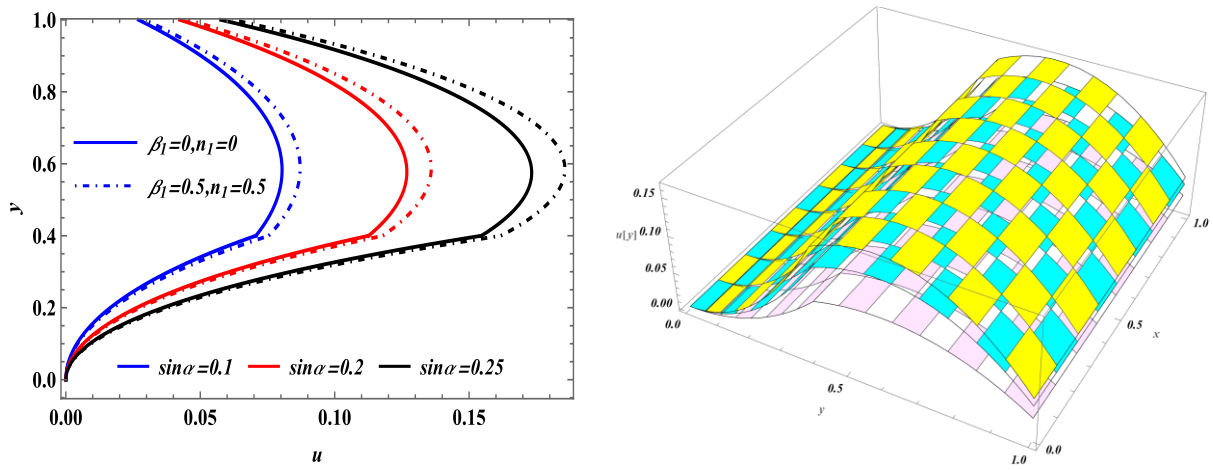

(a)

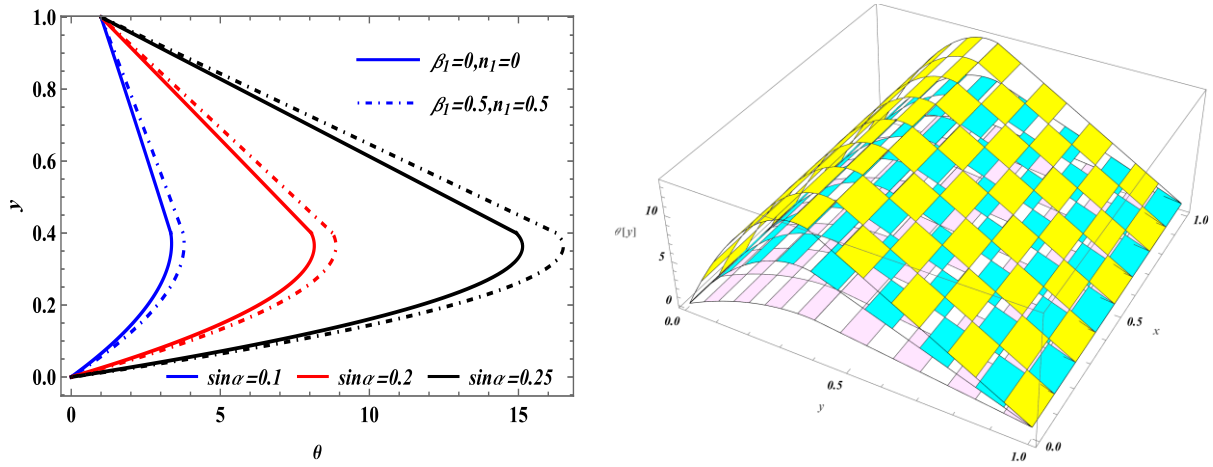

(b)

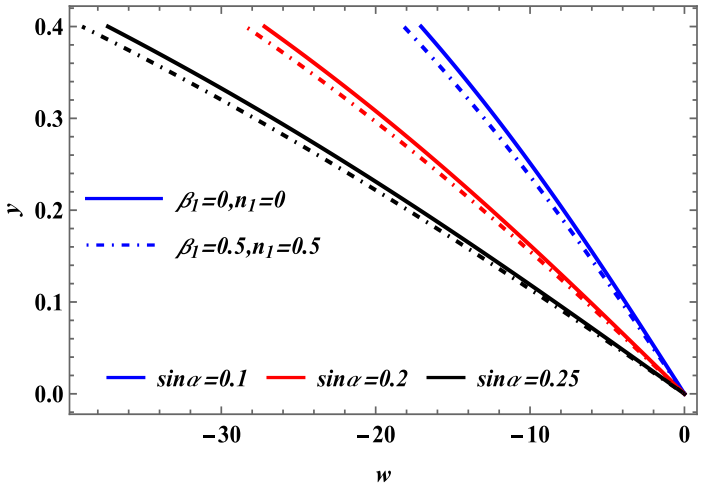

(c)

Fig. 4. Variations of a) Velocity; b) Temprature ; c) Microrotation velocity with $sin\alpha$ for $Fr = 0.2, Da = 0.5, M = 0.5,$ $\mu = 0.5, \varepsilon_1 = 0.6, \beta$=0.4, N=0.2, m=2, a=1, a_1=0.4, Rd=1, Q=1, k=0.5

The relationship between Newtonian and rotational viscosity is represented by the coupling parameter N. As rotational viscosity decreases, this coupling weakens, diminishing the fluid's micropolar characteristics. Thus, when N approaches zero, the flow resembles that of a viscous fluid. In contrast, as the coupling parameter increases, the viscosity associated with rotational motion rises, resulting in a significant reduction in the velocity profile, as shown in Figure 5(a). Figure 5(b) illustrates that with an increase in the coupling number, micro-rotation also rises.

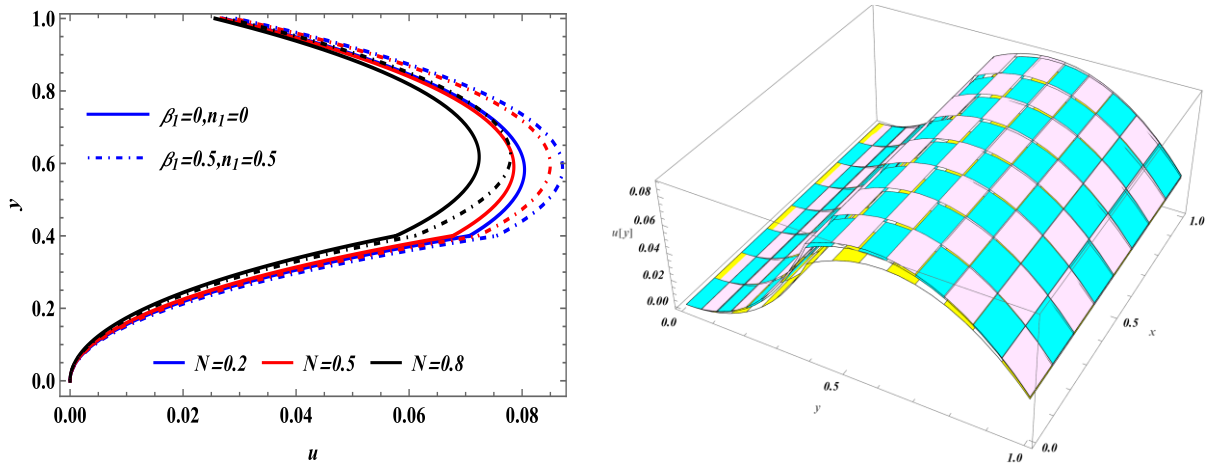

(a)

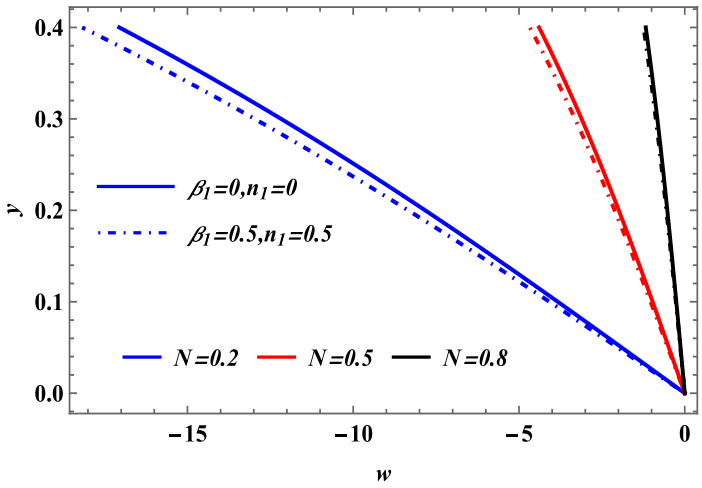

(b)

Fig. 5. Variations of a) Velocity; b) Microrotation velocity with N for $Fr = 0.2, Da = 0.5, M = 1, \mu = 0.5, \varepsilon = 0.5, \varepsilon_1 = 0.6, \beta$=0.4, $sin\alpha$ =0.2, m=2, a=1, a_1=0.4, Rd=1, Q=1, k=0.5

According to Figure 6(a), When fluid particles interact with material elements, drag is reduced, facilitating a decrease in momentum in core region, with the opposite effect in the peripheral region. Conversely, Figure 6(b) exhibits the reverse pattern.

With a rise in the Froude number, inertial forces surpass gravitational forces, leading to a reduction in fluid velocity and a decrease in temperature distribution, as demonstrated in Figures 7(a) and 7(b).

Rising velocity slip enhances velocity in the peripheral region (Figure 8(a)) and also increases the temperature distribution (Figure 8(b)).

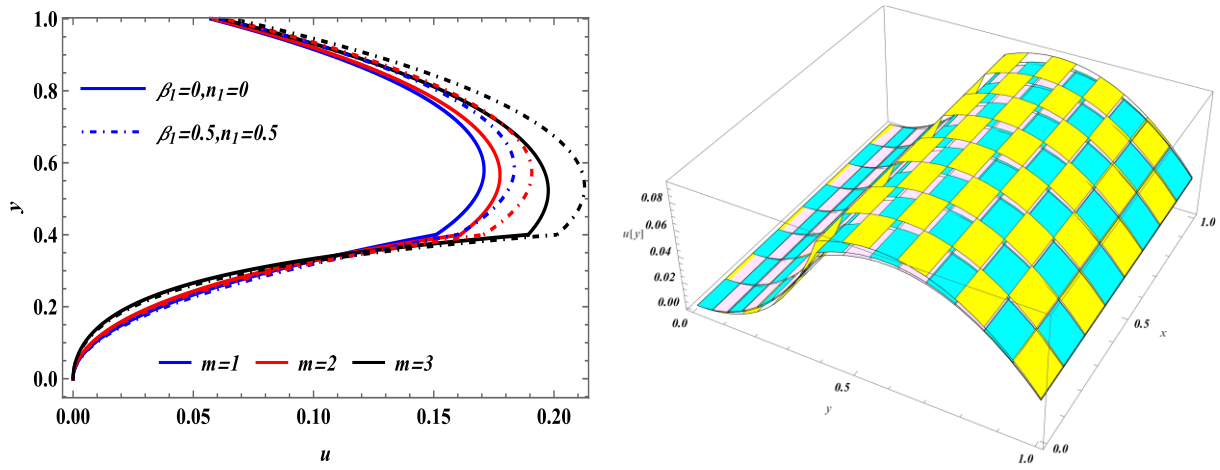

(a)

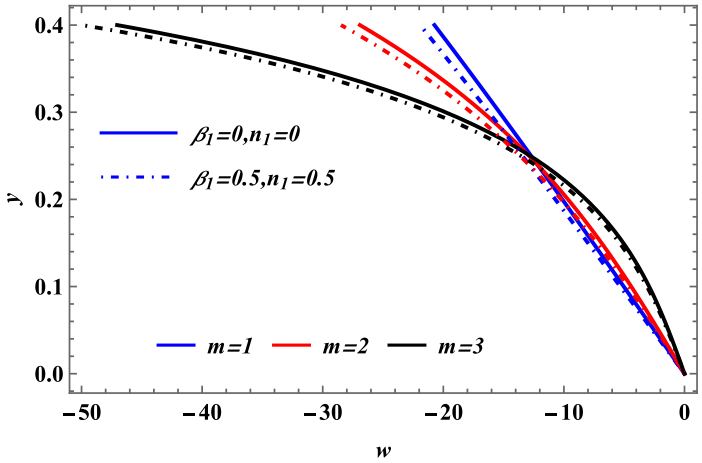

(b)

Fig. 6. Variations of a) Velocity; b) Microrotation velocity with m for $Fr = 0.2, Da = 0.5, M = 1, \mu = 0.5, \varepsilon = 0.5, \varepsilon_1 = 0.6,$ β=0.4, $sin\alpha$ =0.2, N=0.2, a=1, a_1=0.4, Rd=1, Q=1, k=0.5

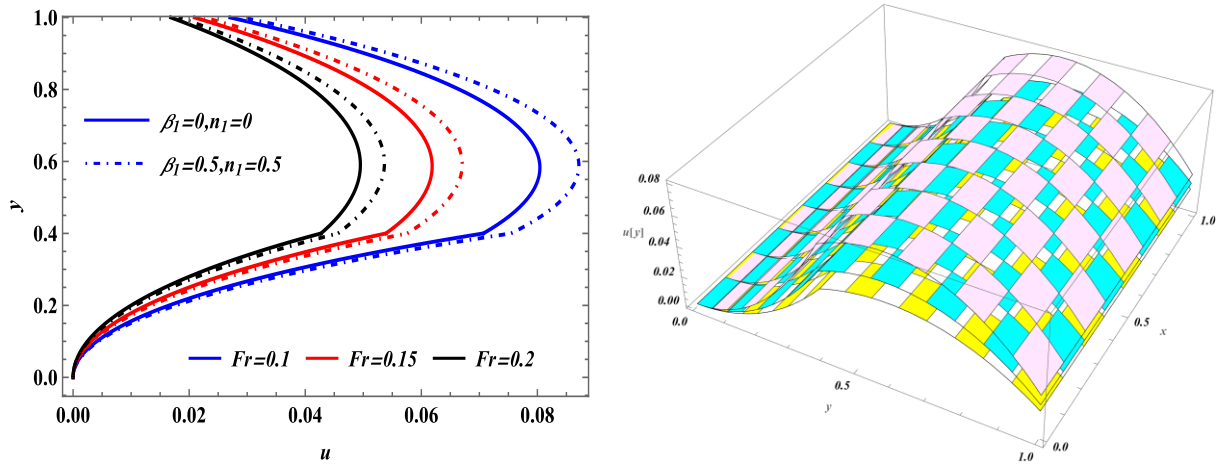

(a)

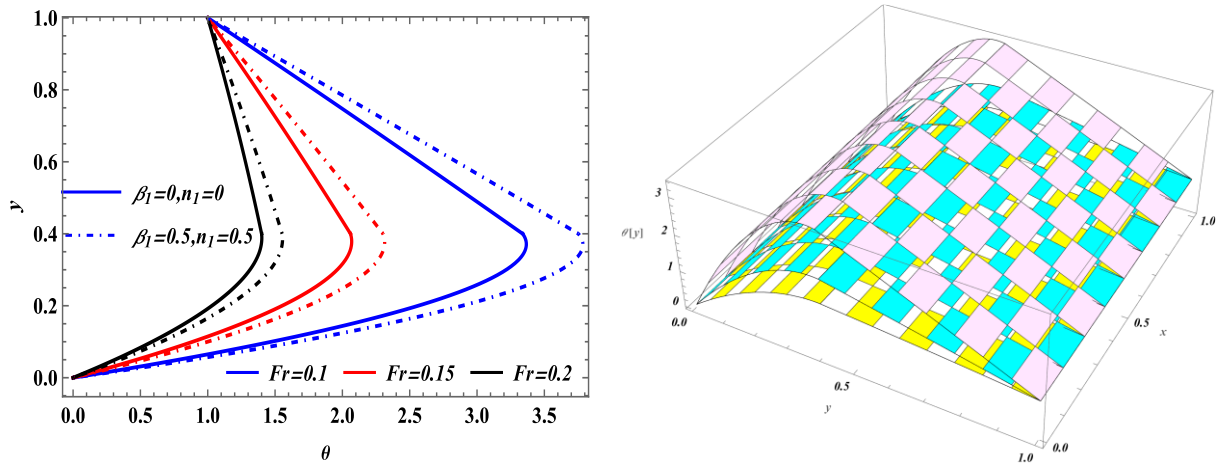

(b)

Fig. 7. Variations of a) Velocity; b) Temprature with FR for $m = 2, Da = 0.5, M = 1, \mu = 0.5, \varepsilon = 0.5, \varepsilon_1 = 0.6,$ β=0.4, $sin\alpha$ =0.2, N=0.2, a=1, a_1=0.4, Rd=1, Q=1, k=0.5

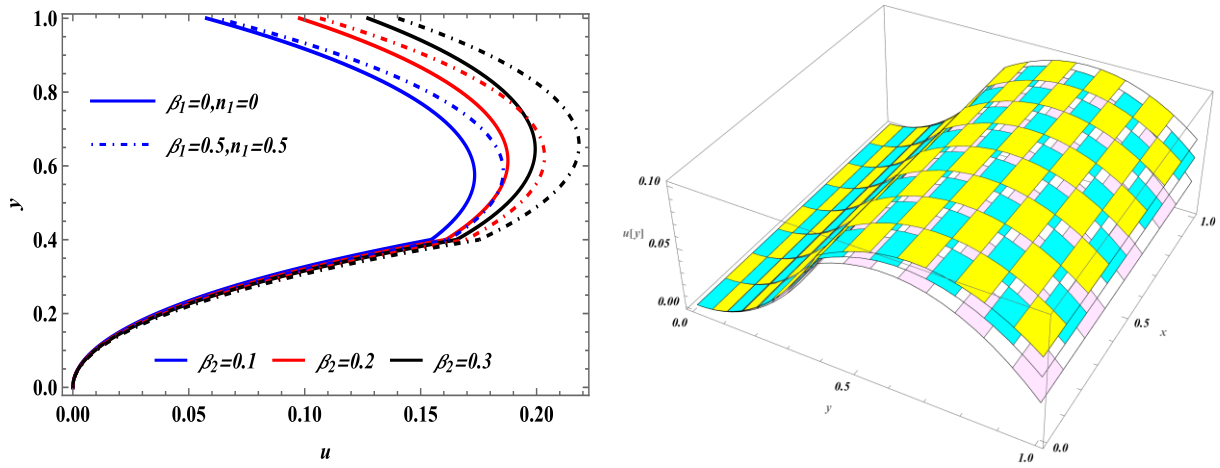

(a)

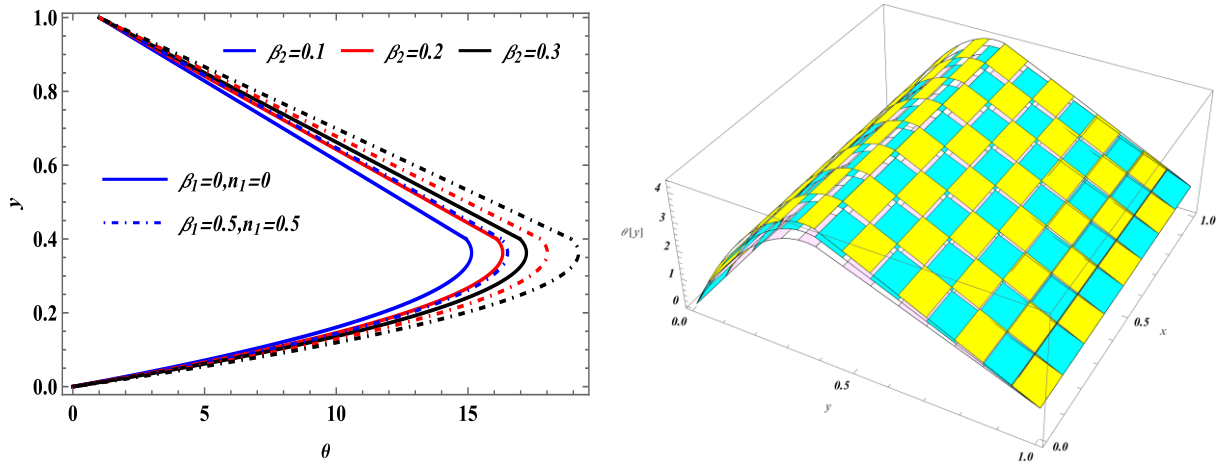

(b)

Fig. 8. Variations of a) Velocity; b) Temprature with β_2 for $m = 2, Da = 0.5, M = 1, \mu = 0.5, \varepsilon = 0.5, \varepsilon_1 = 0.6,$

β=0.4, $sin\alpha$ =0.2, N=0.2, a=1, a_1=0.4, Rd=1, Q=1, k=0.5

A higher value of β indicates a reduction in viscosity or yield stress, leading to an increase in fluid velocity, as depicted in Figure 9(a) and lowering the liquid temperature (9(b)).

From Figure 10(a) one can observe that the mean kinetic energy of the liquid particle rises with the temperature, enhancing the movement and speed of the molecules within the channel. This also leads to reduced spacing between liquid molecules. Physically, an increase in the distribution of the temperature field facilitates heat transfer from a region of heat absorption $(\Upsilon_1 = \Upsilon_2 = \Upsilon < 0)$ to a region of heat generation $(\Upsilon > 0)$. Higher thermal conductivity ratios facilitate more efficient heat conduction throughout the fluid, which in turn reduces the temperature, as depicted in Figure 10(b). From Figure 10(c), it is clear that a higher Brinkman number indicates slower conduction of the generated heat, resulting in a notable temperature increase in the fluid.

Figure 11(a) demonstrates the influence of mass diffusivity on the species concentration profile, indicating an enhancement in concentration with a rise in diffusivity, D. Figure 11(b) illustrates that increasing the chemical reaction parameter reduces the species concentration profile. This decline is due to the thinner solute boundary layer and restricted mass transfer caused by the reaction.

Figure 12(a) and Figure 12(b) shows that an increase in the Sc, and Sr results in reduced mass diffusivity, thereby leading to a decline in concentration.

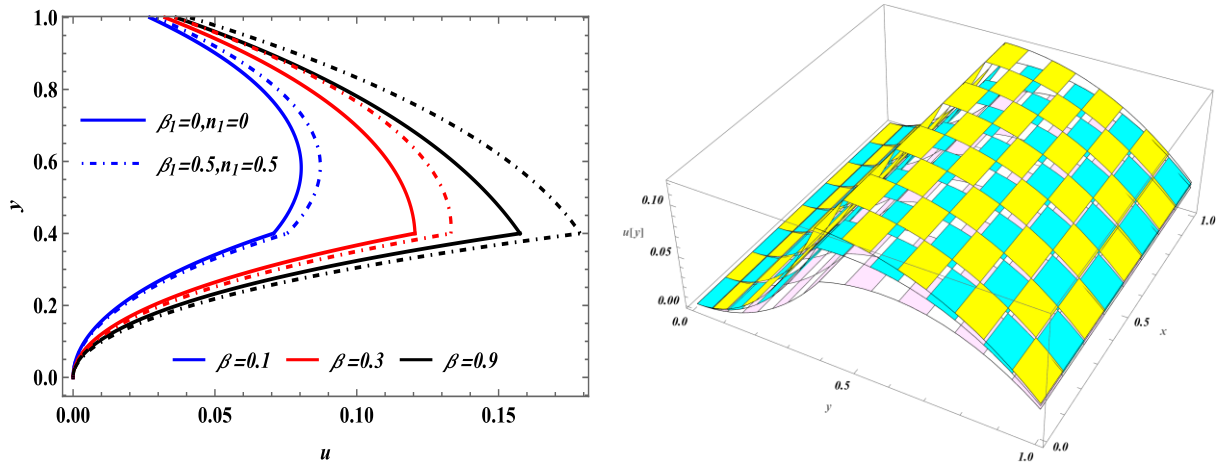

(a)

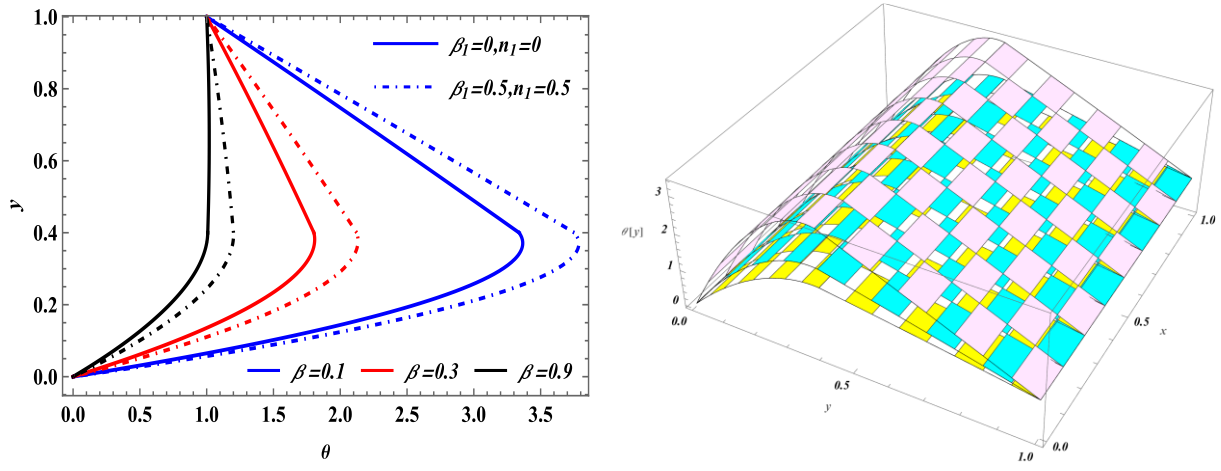

(b)

Fig. 9. Variations of a) Velocity; b) Temprature with β for $m = 2, Da = 0.5, M = 1, \mu = 0.5, \varepsilon = 0.5, \varepsilon_1 = 0.6$, $sin\alpha$ =0.2, N=0.2, a=1, a_1=0.4, Rd=1, Q=1, k=0.5

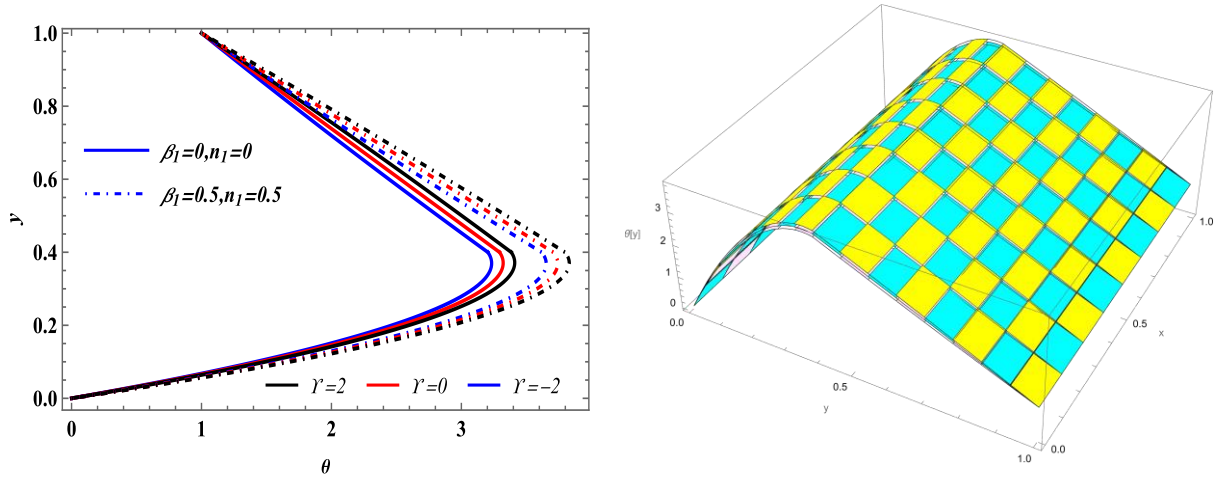

(a)

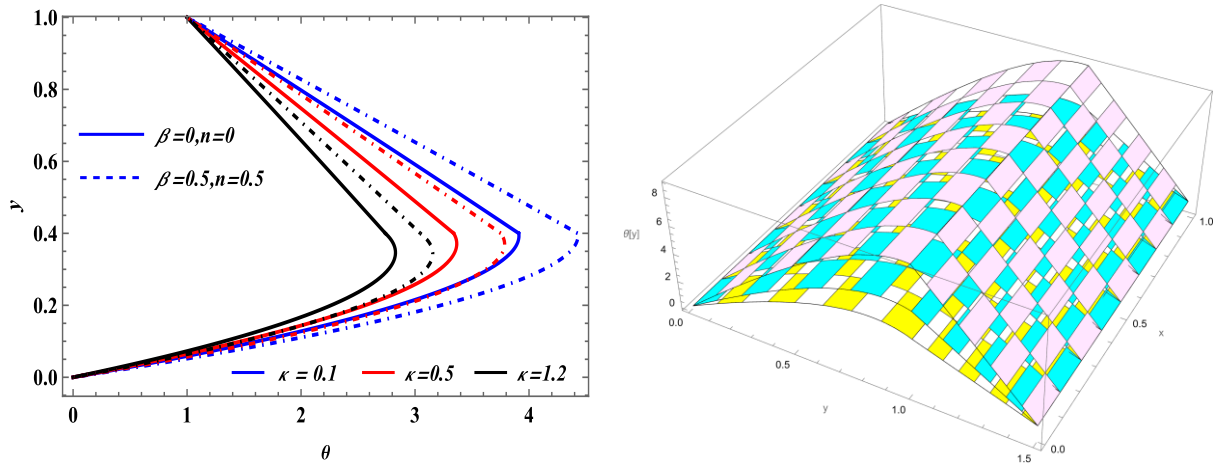

(b)

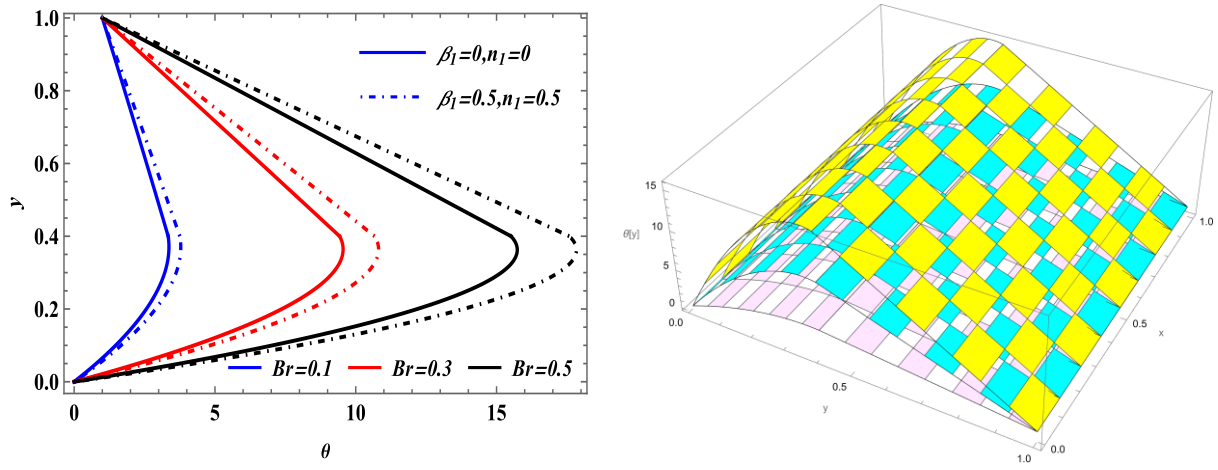

(c)

Fig. 10. Variations of temprature with a) Υ ; b) k; c) Br for $Fr = 0.2, Da = 0.5, M = 1, \mu = 0.5, \varepsilon = 0.5, \varepsilon_1 = 0.6,$ β=0.4, N=0.2, m=2, a=1, a_1=0.4, Rd=1

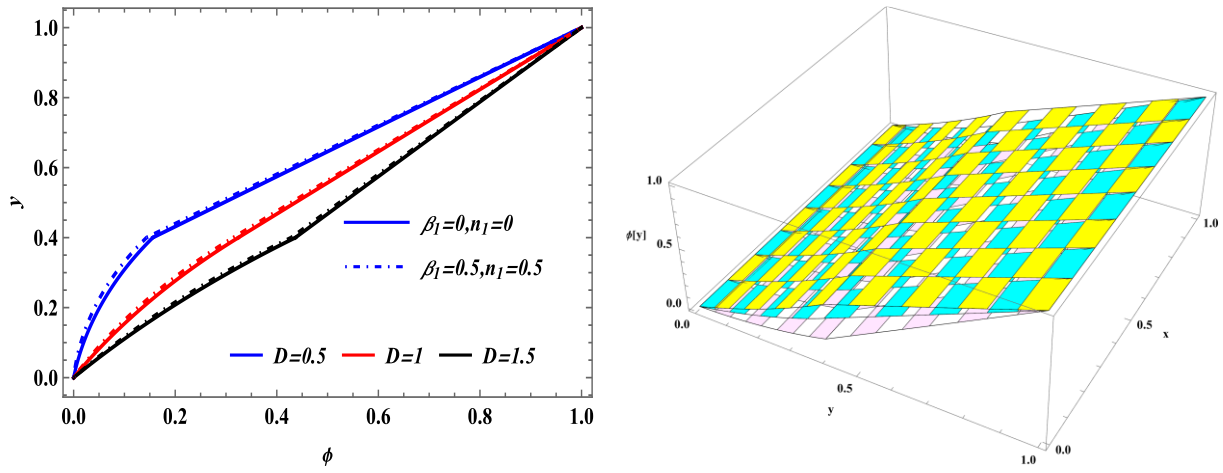

(a)

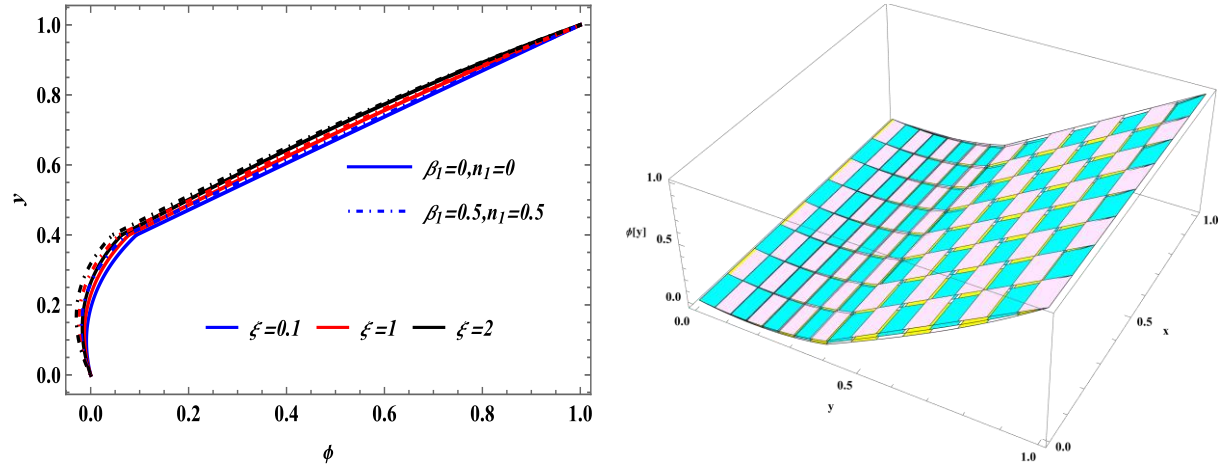

(b)

Fig. 11. Variations of concentration with a) D; b) ξ for $Fr = 0.2, Da = 0.5, M = 1, \mu = 0.5, Sc = 0.3, Sr = 0.5, \varepsilon = 0.5, \varepsilon_1 = 0.6, \beta$=0.4, N=0.2, m=2, a=1, a_1=0.4, Rd=1

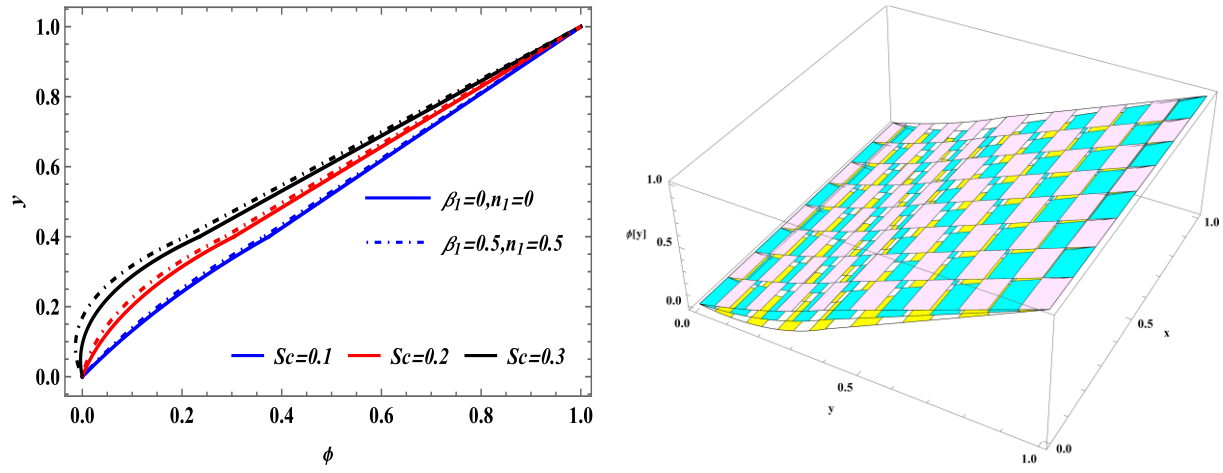

(a)

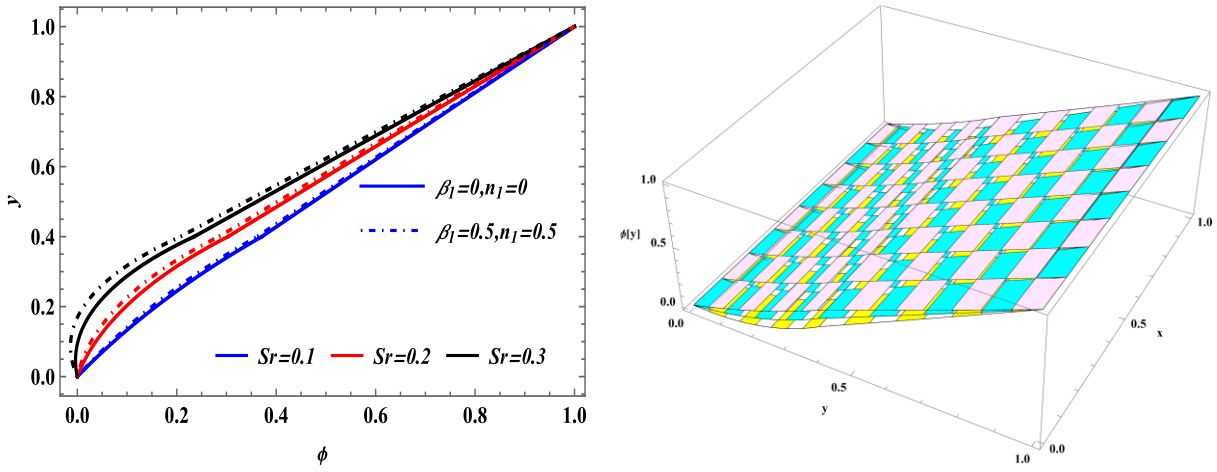

(b)

Fig. 12. Variations of concentration with a) Sc; b) Sr for $Fr = 0.2, Da = 0.5, M = 1, \mu = 0.5, D = 0.5, \xi = 1,$ $\varepsilon = 0.5, \varepsilon_1 = 0.6, \beta$=0.4, N=0.2, m=2, a=1, a_1=0.4, Rd=1

Figure 13 demonstrates the pressure gradient's variation over one wavelength, $x \in [0,1]$. Observably, the pressure gradient is lower in the wider sections of the channel, specifically $x \in [0,0.2]$ and $x \in [0.7,1]$, whereas in the narrower region $x \in [0.2,0.7]$, the pressure gradient increases significantly.

The impact of the N on the pressure gradient is shown in Figure 13(a). For $N = 0$, representing no coupling between the flow field and microrotation, the behavior aligns with that of a Newtonian fluid. As N increases, indicating stronger coupling between flow velocity and micro-rotation, the axial variation in the pressure gradient becomes more pronounced. For micropolar fluids, higher values of N necessitate a larger pressure gradient to maintain a consistent flux rate, with microrotation introducing a resistance effect to the flow. For a Newtonian liquid, the required pressure gradient is minimal. In contrast, the effect of the m on pressure gradient, illustrated in Figure 13(b), shows an opposite trend to that of N. As m rises, the pressure gradient across the wavelength also enhances. This finding is consistent with the fact that a given rate of volume flow is maintained more easily in the wider channel sections without requiring a higher pressure gradient. A similar behavior is observed in Figure 13(c) with an increase in $\sin\alpha$, where the pressure gradient also increases from a horizontal to a vertical channel configuration. Additionally, Figure 13(d) indicates that as the magnetic parameter M enhances, the pressure gradient rises. This suggests that stronger magnetic fields applied to the flow increase the required pressure gradient to sustain flow within the channel, a useful effect for surgical procedures where controlled fluid pressure can help manage blood flow during critical operations. As shown in Figure 13(e), one can witness that a increase in the β makes the liquid more resistant to flow due to higher yield stress and viscosity, which leads to an increase in the pressure gradient required to maintain the flow. Conversely, in Figure 13(f), as the Froude number Fr increases, the pressure gradient trend is the opposite of that observed with M, indicating distinct effects on flow resistance and pressure gradient dynamics for these parameters.

Three sections are identified based on pressure difference: the pumping region $(\Delta p > 0)$, the co-pumping region $(\Delta p < 0)$, and the free pumping region $(\Delta p = 0)$. For varying values of the coupling number N, Figure 14(a) shows that the pumping effect for a micropolar liquid exceeds that of a Newtonian liquid. As N increases, the pumping efficiency improves, indicating that a higher coupling number enhances peristaltic pumping by counteracting pressure resistance and driving flow more effectively. In Figure 14(b), changes in the micropolar parameter m position the pumping curves of the micropolar liquid above those of the Newtonian fluid, reinforcing the enhanced pumping effect in fluid. However, as shown in Figure 14(c), the pumping effect diminishes with an increase in the angle of inclination $\sin\alpha$. Additionally, Figures 14(d), 14(e), and 14(f) illustrate that with increases in the magnetic parameter M, Casson parameter, and Froude number Fr, the pressure rise intensifies, indicating a higher pressure required to maintain flow under these conditions.

Figure 15(a) to Figure 15(f) depict how frictional forces vary with changes in the volume flow rate for different parameters. Notably, the frictional forces follow a reverse pattern in comparison to the pressure rise.

Figure 16 illustrates about the Mechanical efficiency of the Casson-micropolar fluid. Mechanical efficiency rises with the rise of micro-rotation, micropolar liquid parameter, Fr, and M parameters, whereas mechanical efficiency falls with the rise of $\sin\alpha$, β.

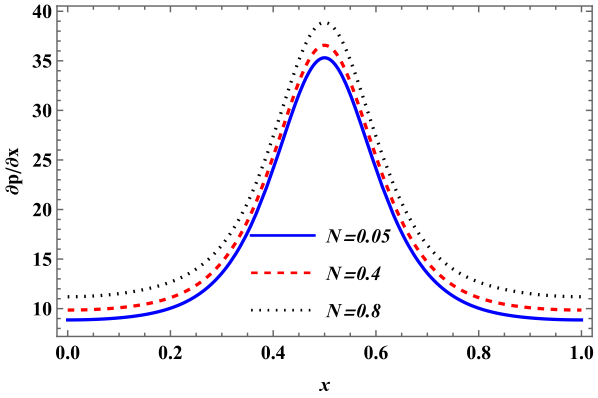

(a) Variable N for
$sin\alpha = 0.2,\ Fr = 0.2,\ M = 1, \mu = 0.5,$
$Da = 0.5, \varepsilon = 0.5, \varepsilon_1 = 0.6, \beta$=0.4, a=1, a₁=0.4

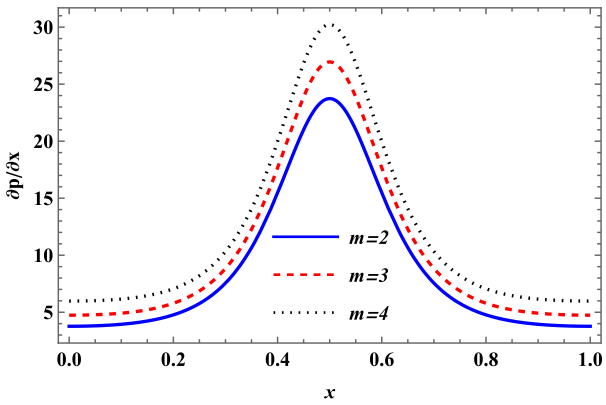

(b) Variable m for
$sin\alpha = 0.2,\ Fr = 0.2,\ Da = 0.5,\ M = 1,$
$Fr = 0.2, \mu = 0.5, \varepsilon = 0.5, \varepsilon_1 = 0.6, \beta$=0.4, a=1, a₁=0.4

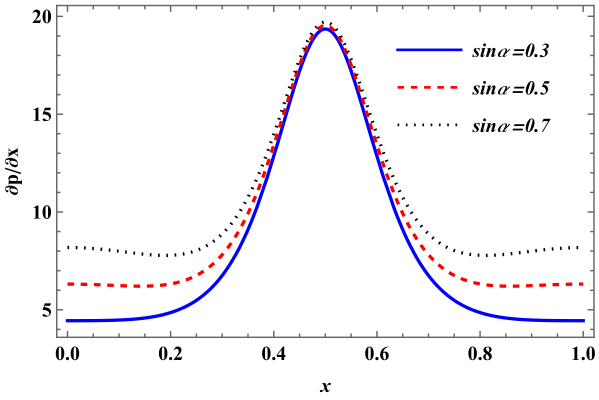

(c) Variable $sin\alpha$ for
$Da = 0.5, M = 0.5, Fr = 0.2, \mu = 0.5,$
$\varepsilon = 0.5, \varepsilon_1 = 0.6, N$=0.2, a=1, a₁=0.4

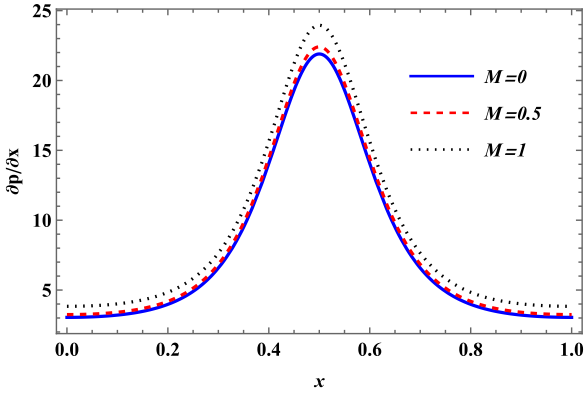

(d) Variable M for
$sin\alpha = 0.2, Fr = 0.1, Da = 0.5, \mu = 0.5,$
$\varepsilon = 0.5, \varepsilon_1 = 0.6, N$=0.2, a=1, a₁=0.4

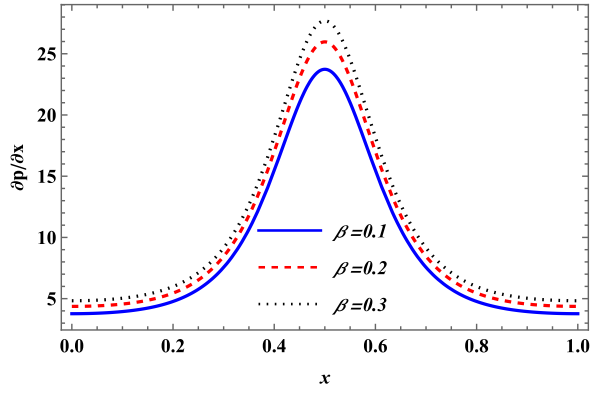

(e) Variable β for
$sin\alpha = 0.2, Fr = 0.2, Da = 0.5, M = 0.5, \mu = 0.5,$
$\varepsilon = 0.5, \varepsilon_1 = 0.6, N$=0.2, a=1, a₁=0.4

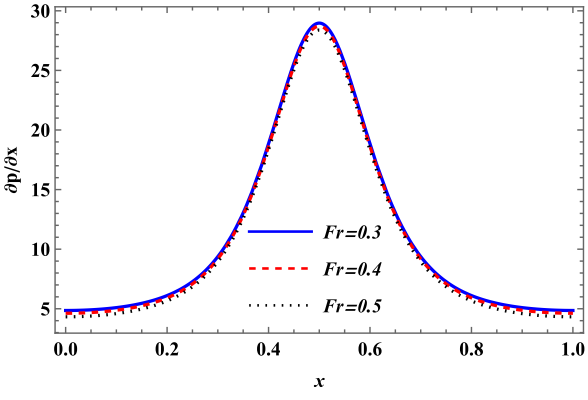

(f) Variable Fr for
$sin\alpha = 0.2, Da = 0.5, M = 1, \mu = 0.5,$
$\varepsilon = 0.5, \varepsilon_1 = 0.6, N$=0.2, a=1, a₁=0.4

Fig. 13. Pressure gradient profiles for different parameters

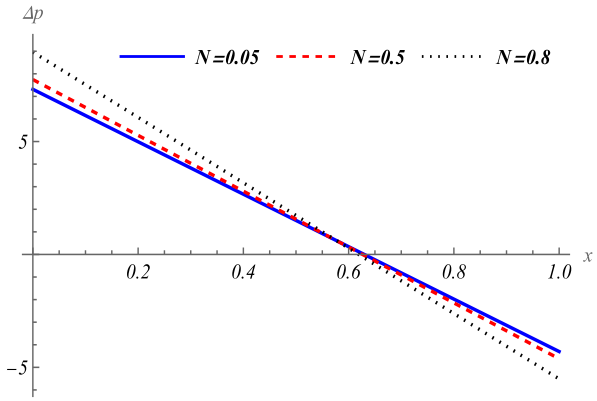

(a) Variable N for

$sin\alpha = 0.2, Fr = 0.2, Da = 0.5, M = 1, \mu = 0.5, D = 0.5, \varepsilon = 0.5, \varepsilon_1 = 0.6, \beta$=0.4, a=1, a₁=0.4

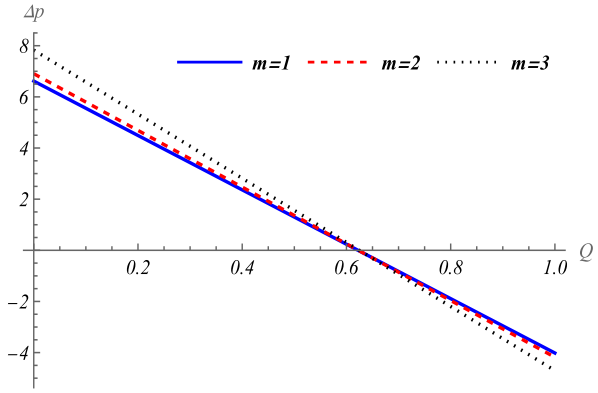

(b) Variable m for

$sin\alpha = 0.2, Fr = 0.2, Da = 0.5, M = 1, \mu = 0.5, \varepsilon = 0.5, \varepsilon_1 = 0.6, \beta$=0.4, a=1, a₁=0.4

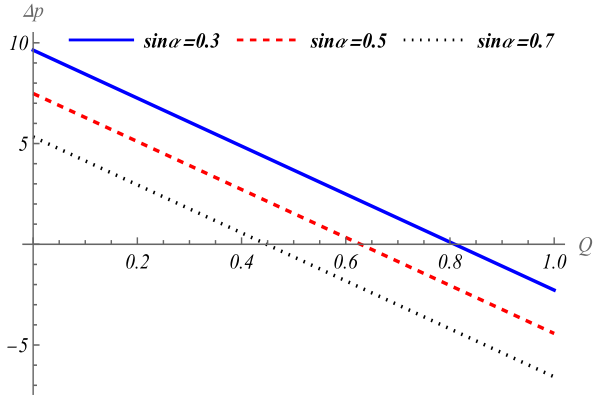

(c) Variable $sin\alpha$ for

$Da = 0.5$, $Fr = 0.2$, $\mu = 0.5$, $\varepsilon = 0.5, \varepsilon_1 = 0.6, N$=0.2, a=1, a₁=0.4

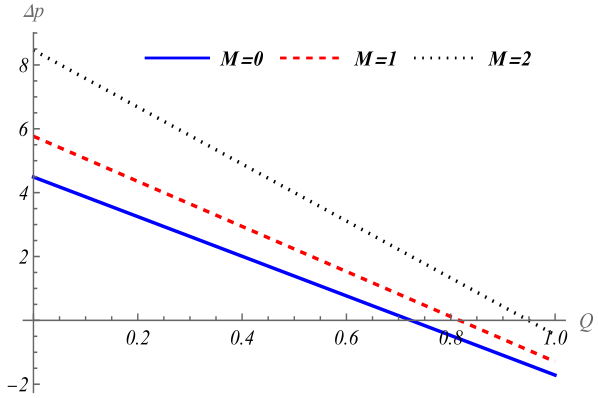

(d) Variable M for

$sin\alpha = 0.2$, $m = 2$, $Da = 0.5$, $\mu = 0.5$, $\varepsilon = 0.5$, $\varepsilon_1 = 0.6$, N=0.2, a=1, a₁=0.4

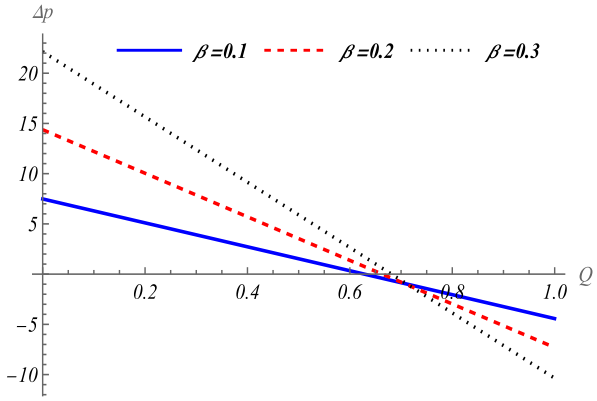

(e) Variable β for

$M = 1, m = 2, Da = 0.5, M = 0.5, sin\alpha = 0.2, \mu = 0.5, \varepsilon = 0.5, \varepsilon_1 = 0.6, N$=0.2, a=1, a₁=0.4

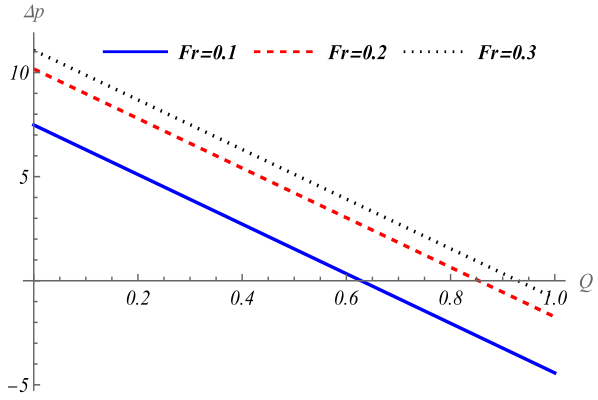

(f) Variable Fr for

$sin\alpha = 0.5, Da = 0.5, M = 1, \mu = 0.5, \varepsilon = 0.5, \varepsilon_1 = 0.6, N$=0.2, a=1, a₁=0.4

Fig. 14. Pressure rises for different parameters

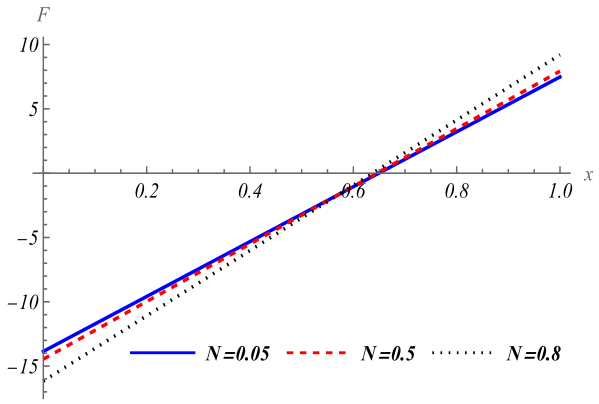

(a) Variable *N* for
$sin\alpha = 0.2, Fr = 0.2, Da = 0.5, M = 1, \mu = 0.5,$
$\varepsilon = 0.5, \varepsilon_1 = 0.6, \beta$=0.4, a=1, a_1=0.4

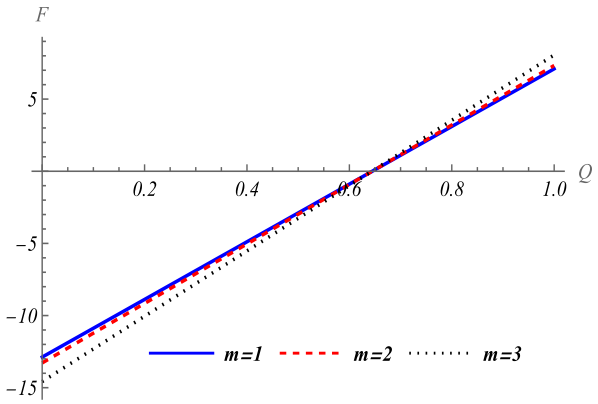

(b) Variable *m* for
$sin\alpha = 0.2, Fr = 0.2, Da = 0.5, M = 1, Fr = 0.2,$
$\mu = 0.5, \varepsilon = 0.5, \varepsilon_1 = 0.6, \beta$=0.4, a=1, a_1=0.4

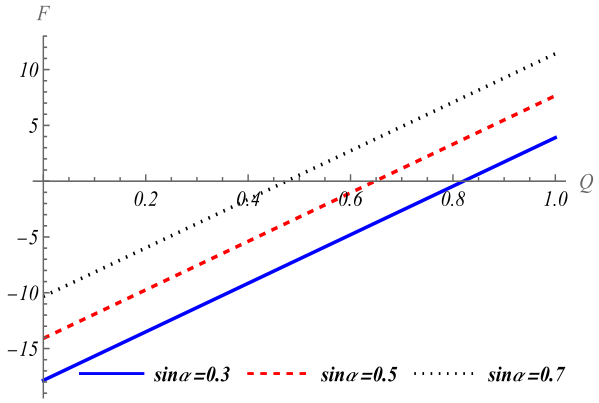

(c) Variable $sin\alpha$ for
$Da = 0.5, M = 0.5, Fr = 0.2, \mu = 0.5,$
$\varepsilon = 0.5, \varepsilon_1 = 0.6, N$=0.2, a=1, a₁=0.4

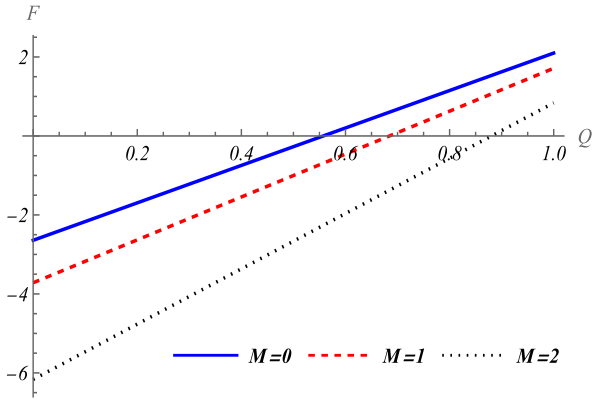

(d) Variable *M* for
$sin\alpha = 0.2, Fr = 0.1, Da = 0.5, \mu = 0.5,$
$\varepsilon = 0.5, \varepsilon_1 = 0.6, N$=0.2, a=1, a_1=0.4

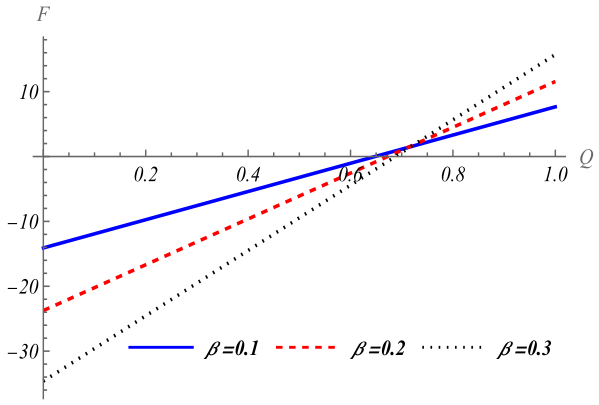

(e) Variable β for
$sin\alpha = 0.2, m = 2, Da = 0.5, M = 1, \mu = 0.5,$
$\varepsilon = 0.5, \varepsilon_1 = 0.6, N$=0.2, a=1, a₁=0.4

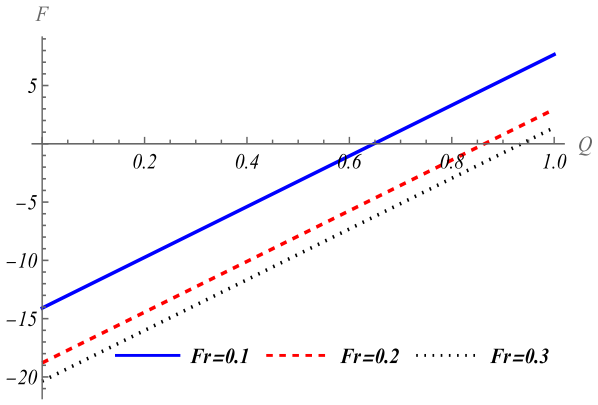

(f) Variable *Fr* for
$sin\alpha = 0.5, Da = 0.5, M = 1, \mu = 0.5,$
$\varepsilon = 0.5, \varepsilon_1 = 0.6, N$=0.2, a=1, a_1=0.4

Fig. 15. Friction forces for different parameters

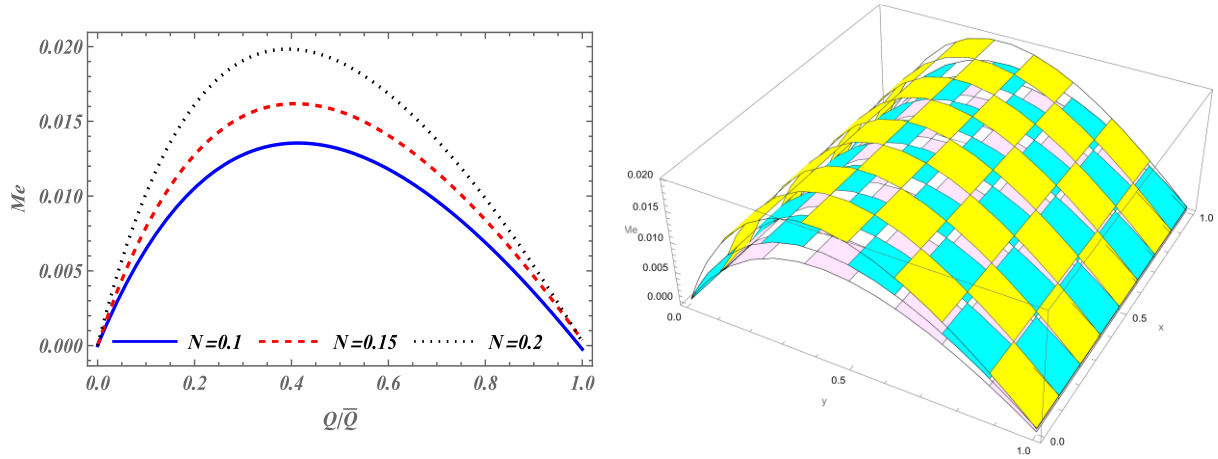

(a) Variable N for

$sin\alpha = 0.2, Fr = 0.2, Da = 0.5, M = 1, \mu = 0.5, \varepsilon = 0.5, \varepsilon_1 = 0.6, \beta$=0.4, a=1, a_1=0.4

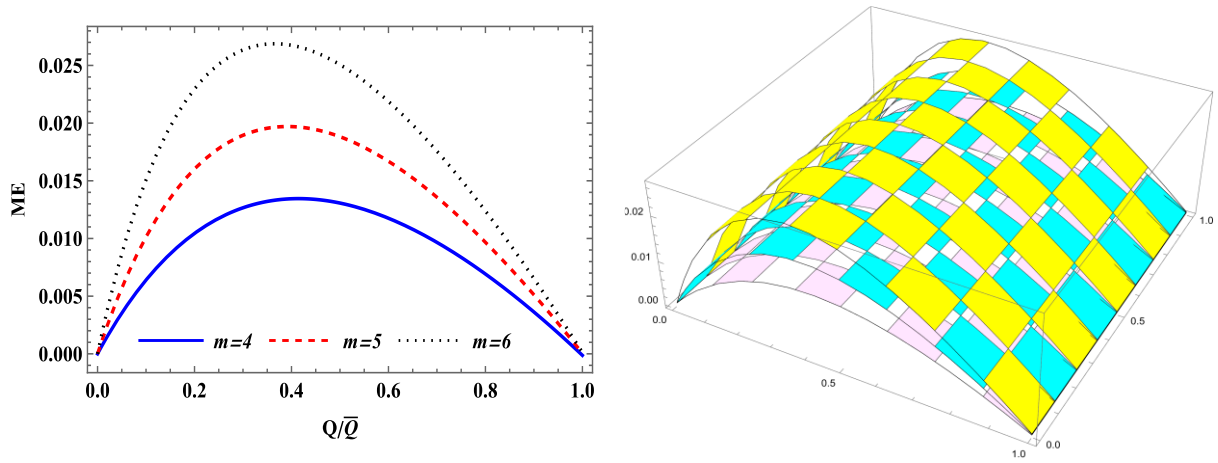

(b) Variable m for

$sin\alpha = 0.2, Fr = 0.2, Da = 0.5, M = 1, Fr = 0.2, N = 0.2, \mu = 0.5, \varepsilon = 0.5, \varepsilon_1 = 0.6, \beta$=0.4, a=1, a_1=0.4

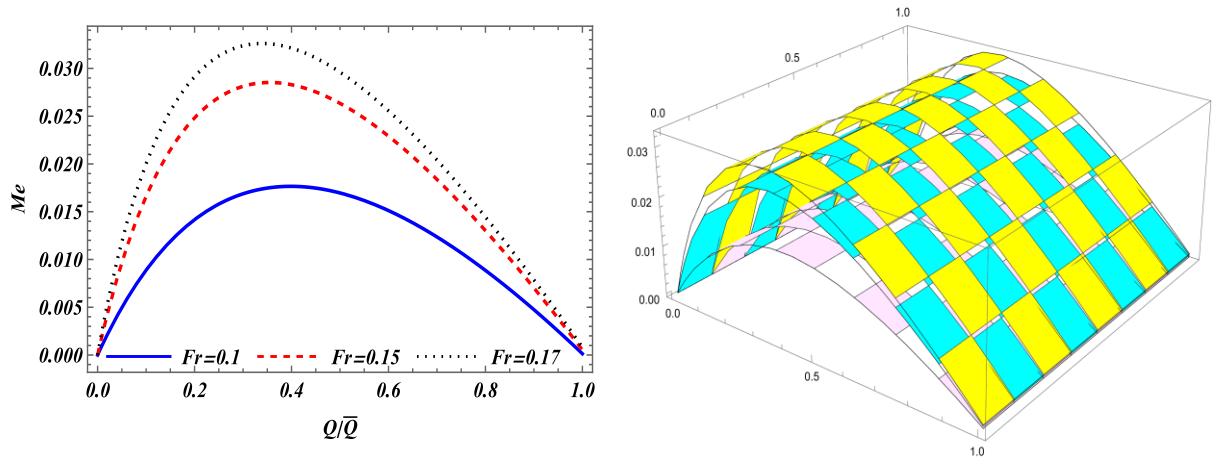

(c) Variable Fr for

$sin\alpha = 0.2, Da = 0.5, M = 1, \mu = 0.5, m = 2, \varepsilon = 0.5, \varepsilon_1 = 0.6, N$=0.2, a=1, a_1=0.4

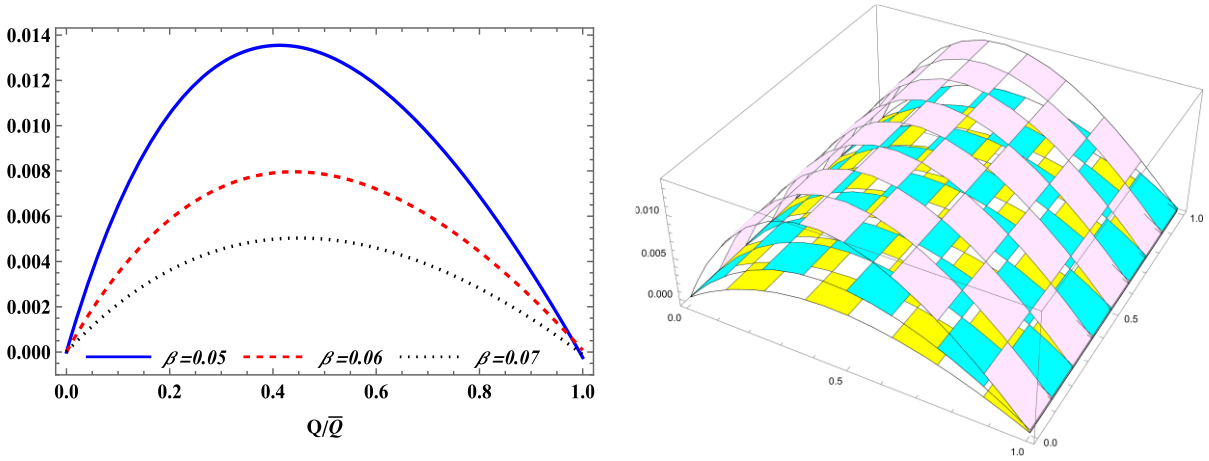

(d) Variable β for

$sin\alpha = 0.2, Fr = 0.2, Da = 0.5, M = 1, m = 2, \mu = 0.5, \varepsilon = 0.5, \varepsilon_1 = 0.6, N$=0.2, a=1, a_1=0.4

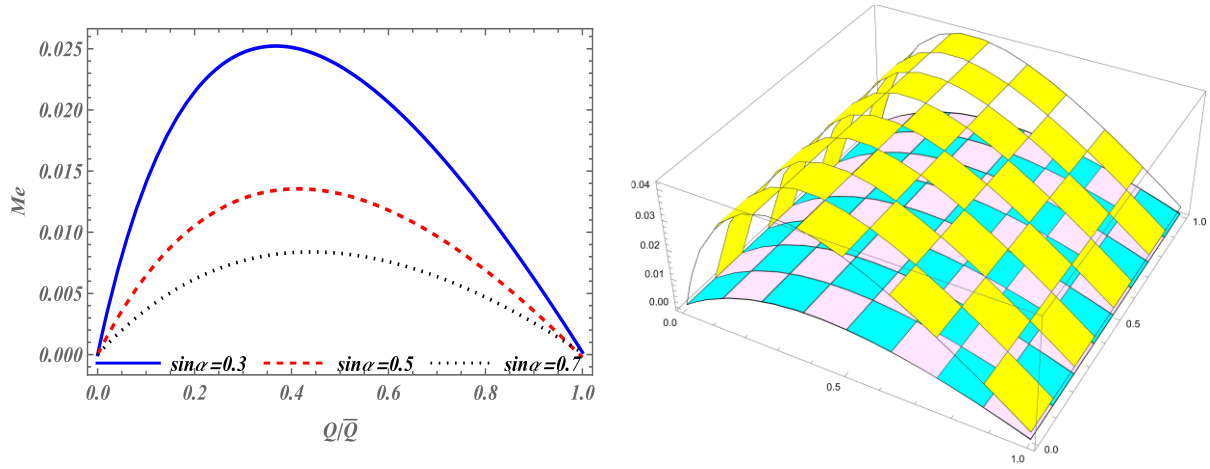

(e) Variable $sin\alpha$ for

$Fr = 0.2, m = 2, Da = 0.5, M = 1, \beta = 0.4, Fr = 0.2, \mu = 0.5, \varepsilon = 0.5, \varepsilon_1 = 0.6, N$=0.2, a=1, a_1=0.4

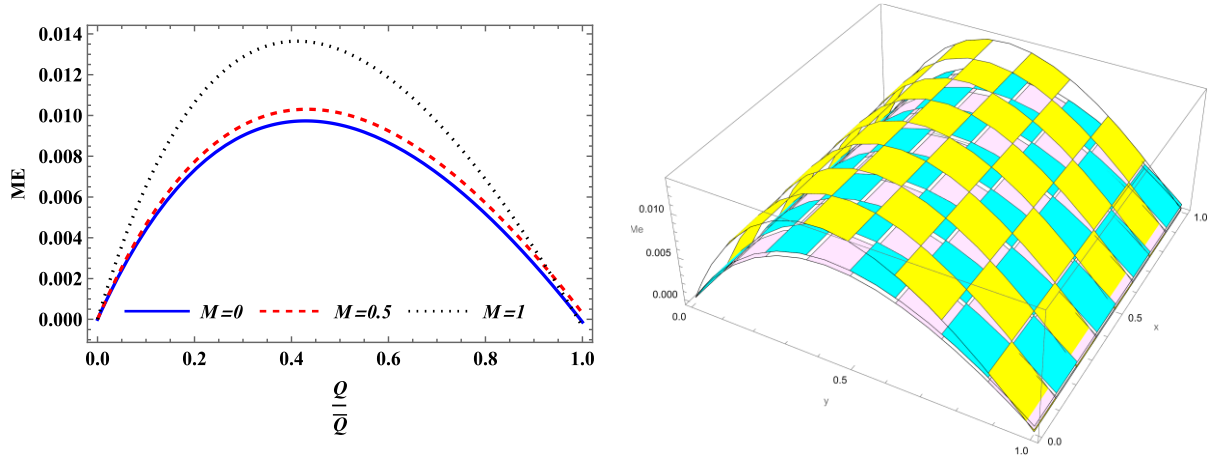

(f) Variable M for

$sin\alpha = 0.2, Fr = 0.2, Da = 0.5, m = 2, \beta = 0.4, \mu = 0.5, \varepsilon = 0.5, \varepsilon_1 = 0.6, N$=0.2, a=1, a_1=0.4

Fig. 16. Mechanical efficiencies for different parameters

Figures 17 and 18 illustrate the variations in entropy generation and the Bejan number as the parameters are varied.

In Figure 17(a), it is observed that, with increasing *N*, entropy generation remains relatively unchanged at the channel centre but declines sharply toward the channel walls. In contrast, the Bejan number exhibits an upward trend, as illustrated in Figure 18(a).

Figure 17(b) indicates that a rise in the magnetic field parameter enhances entropy generation, as the higher magnetic field induces a resistive Lorentz force, resulting in greater friction during fluid flow and, consequently, an increased total entropy generation rate near the channel walls. The Bejan number in Figure 18(b) displays both ascending and descending trends, reflecting the strong influence of fluid friction irreversibility over heat transfer irreversibility.

As fluid temperature rises with increasing inclination angle, Figure 17(c) shows that entropy generation also rises, while Figure 18(c) shows a decrease in the Bejan number with increasing $sin\alpha$.

Figure 17(d) reveals that, an increase in Brinkman number Br leads to a fall in thermal conductivity and enhancement in entropy generation. As observed in Figure 18(d), the Bejan number behaves oppositely to the rate of entropy generation.

Figure 19 illustrates the variation in the Nusselt number with changes in M , Br , and Υ .

As depicted in Figure 19(a), the heat transfer rate strengthens across both regions as M rises. Figure 19(b) indicates that the core region shows negligible change, while the peripheral region displays a reduction in the Nusselt number as Br varies. Figure 19(c) reveals that the heat generation parameter causes the core region to rise, but the peripheral region shows a downward trend.

In Figure 20, the impact of parameters Sc , Sr , D and ξ on the Sherwood number is displayed.

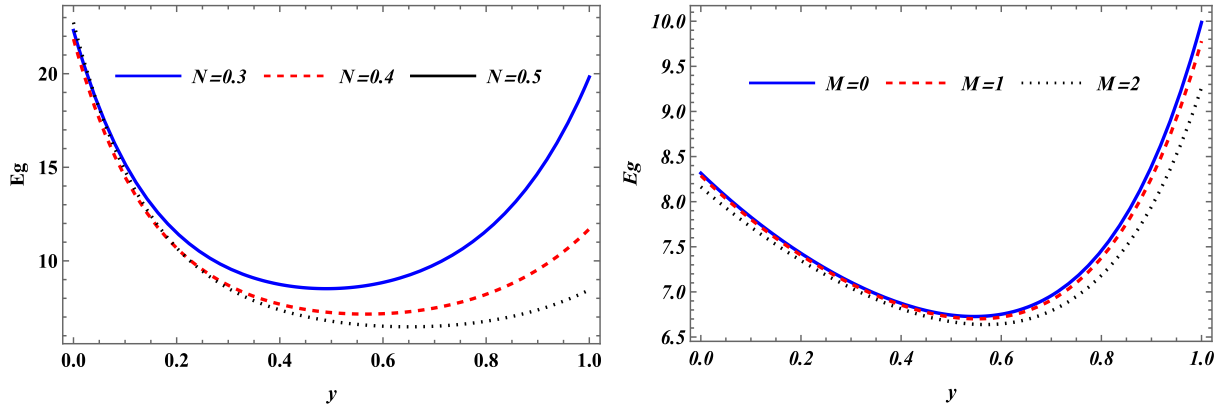

(a) Variable *N* for

$sin\alpha = 0.2, Fr = 0.2, Da = 0.5, M = 1, \mu = 0.5, m = 2, \varepsilon = 0.5, \varepsilon_1 = 0.6$, **$\beta$=0.4, a=1, a_1=0.4, *Rd*=1, *Q*=1, *k*=0.5, *Br*=0.2**

(b) Variable M for

$sin\alpha = 0.2, Fr = 0.2, Da = 0.5, \mu = 0.5, m = 2, \varepsilon = 0.5, \varepsilon_1 = 0.6$, **$\beta$=0.4, a=1, a_1=0.4, *Rd*=1, *Q*=1, *k*=0.5, *Br*=0.2**

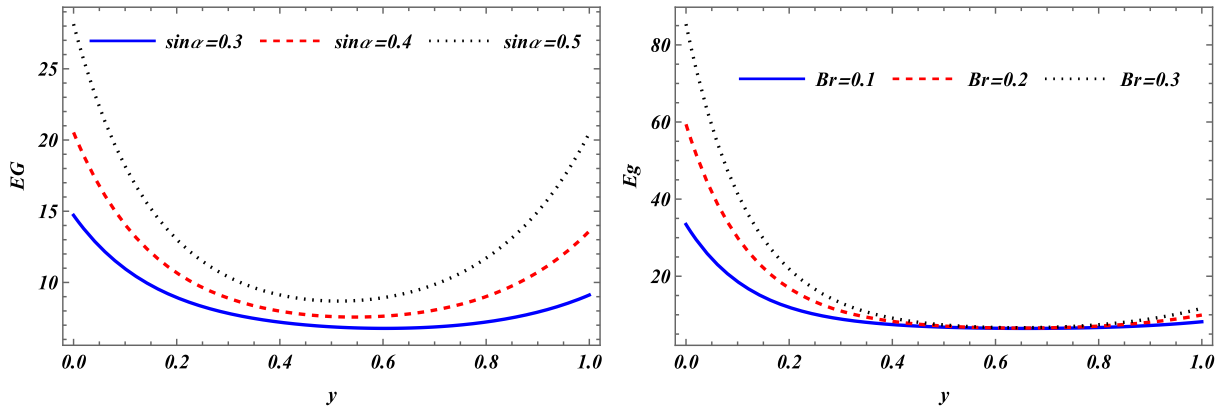

(c) Variable $sin\alpha$ for

$N = 0.2, Fr = 0.2, Da = 0.5, M = 1$, ***Rd*=1, *Q*=1, *k*=0.5, *Br*=0.2, *Sr*=0.5**

(d) Variable *Br* for

$N = 0.2, Fr = 0.2, Da = 0.5, M = 1$, ***Rd*=1, *Q*=1, *k*=0.5, *Sc*=0.3, *Sr*=0.5,** $sin\alpha = 0.2$

Fig. 17. Entropy profiles for different parameters

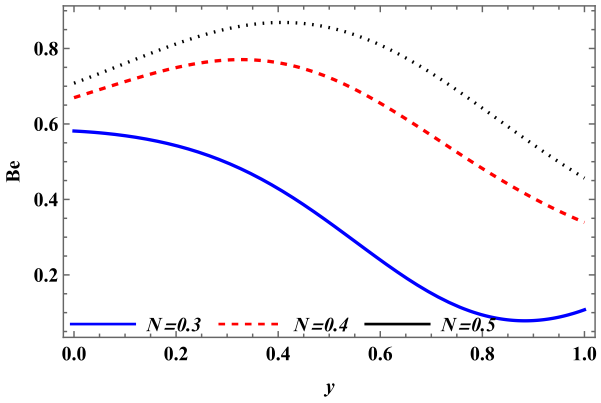

(a) Variable *N* for

$Fr = 0.2, Da = 0.5, M = 1, m = 2$, *Sr*=0.5, *Sc*=0.3, *Rd*=1, *Q*=1, *k*=0.5, *Br*=0.2

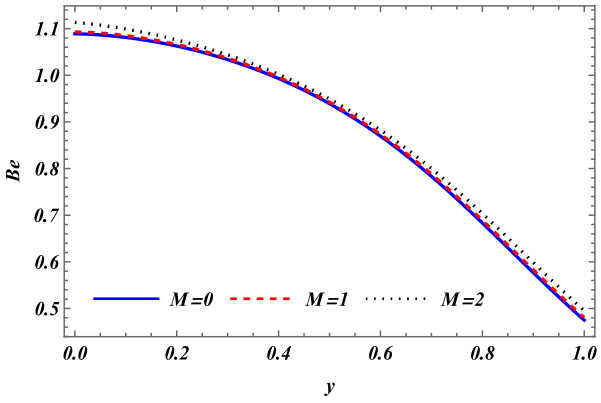

(b) Variable *M* for

$Fr = 0.2, Da = 0.5, N = 0.2, m = 2$, *Sr*=0.5, *Sc*=0.3, *Rd*=1, *Q*=1, *k*=0.5, *Br*=0.2, $sin\alpha = 0.2$

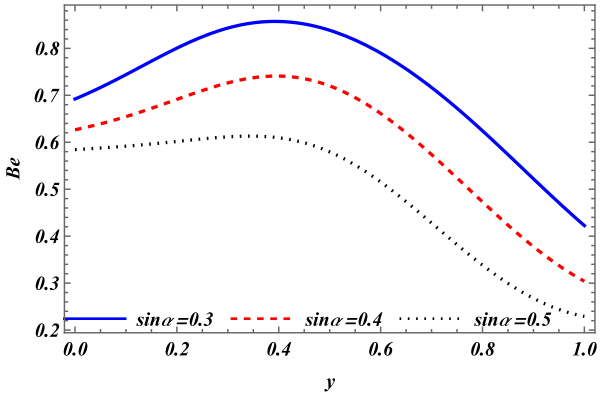

(c) Variable $sin\alpha$ for

$Fr = 0.2, Da = 0.5, N = 0.2, M = 1$, *Sr*=0.5, *Sc*=0.3, *Rd*=1, *Q*=1, *k*=0.5, *Br*=0.2

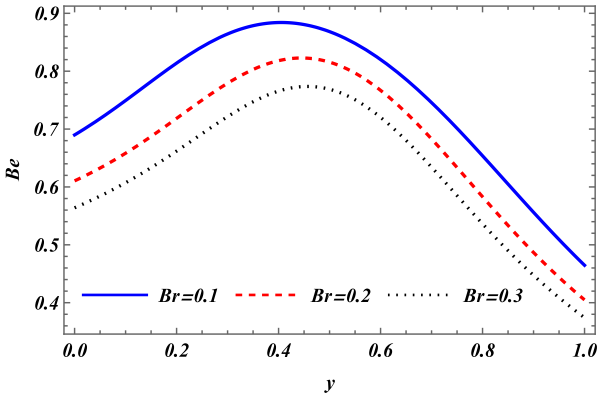

(d) Variable *Br* for

$sin\alpha = 0.2, Fr = 0.2, Da = 0.5, N = 0.2, M = 1$, *Sr*=0.5, *Sc*=0.3, *Rd*=1, *Q*=1, *k*=0.5

Fig. 18. Bejan numbers for different parameters

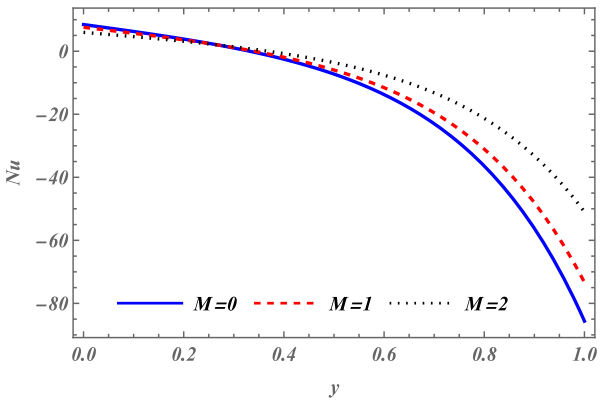

(a) Variable *M* for

$sin\alpha = 0.2, Fr = 0.2, Da = 0.5, m = 2, \beta = 0.4, \mu = 0.5, \varepsilon = 0.5, \varepsilon_1 = 0.6$, *N*=0.2, *Rd*=1, a_1=0.4, γ=1

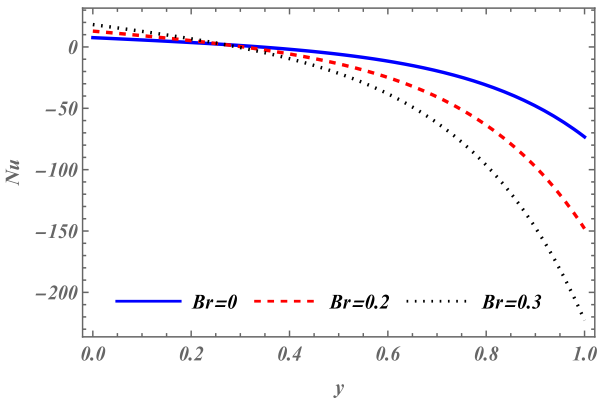

(b) Variable *Br* for

$sin\alpha = 0.2, Fr = 0.2, Da = 0.5, m = 2, \beta = 0.4, \mu = 0.5, \varepsilon = 0.5, \varepsilon_1 = 0.6$, *N*=0.2, *Rd*=1, a_1=0.4, γ=1

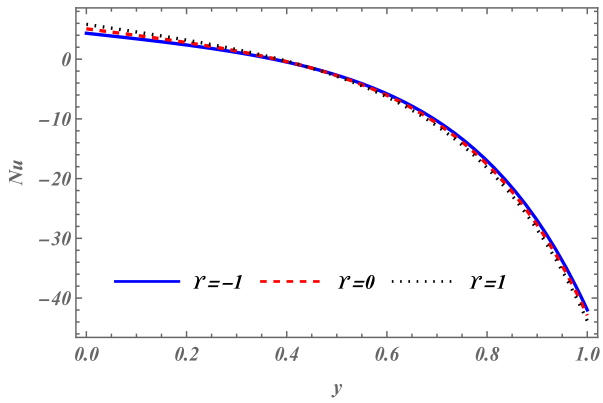

(c) Variable γ for

$sin\alpha = 0.2, Fr = 0.2, Da = 0.5, m = 2, \beta = 0.4, \mu = 0.5, \varepsilon = 0.5, \varepsilon_1 = 0.6$, N=0.2, Rd=1, a_1=0.4, M=0.5

Fig. 19. Nusselt number profiles for different parameters

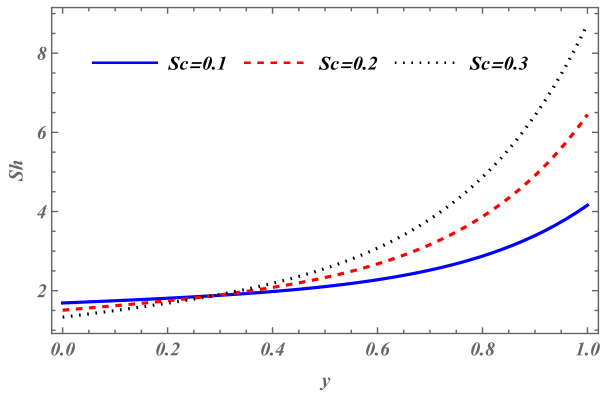

(a) Variable *Sc* for

$sin\alpha = 0.2, Fr = 0.2, Da = 0.5, M = 1, \mu = 0.5, \varepsilon = 0.5, \varepsilon_1 = 0.6$, β=0.4, a=1, a_1=0.4, m=2, Rd=1, Q=1, k=0.5, Sr=0.5, D=1.2, ζ=0.5

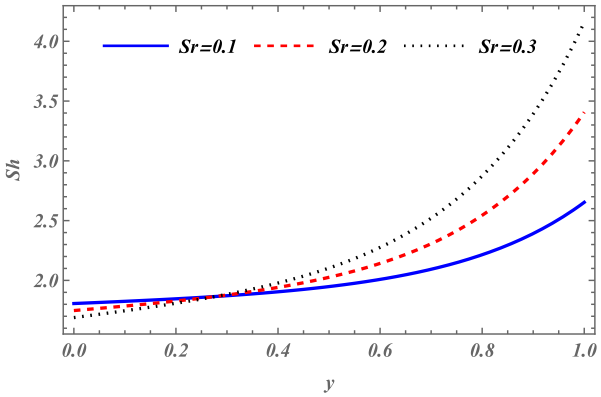

(b) Variable *Sh* for

$sin\alpha = 0.2, Fr = 0.2, Da = 0.5, M = 1, \mu = 0.5, \varepsilon = 0.5, \varepsilon_1 = 0.6$, β=0.4, a=1, a_1=0.4, m=2, Rd=1, Q=1, k=0.5, Sr=0.5, Sc=0.5, D=1.2, ζ=0.5

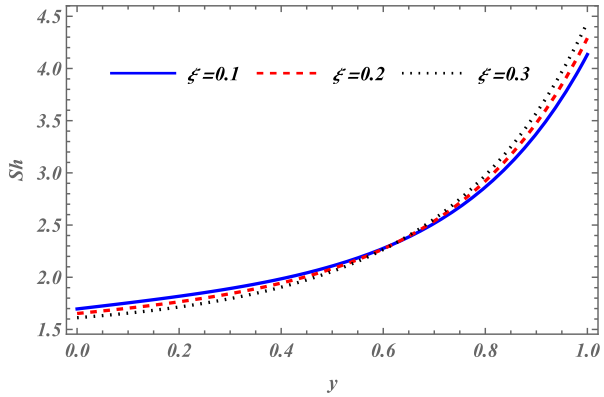

(c) Variable ζ for

$sin\alpha = 0.2, Fr = 0.2, Da = 0.5, M = 1, \mu = 0.5, D = 0.5, \varepsilon = 0.5, \varepsilon_1 = 0.6$, β=0.4, a=1, a_1=0.4, m=2, Rd=1, Q=1, k=0.5, Sr=0.5, Sc=0.5, D=1.2

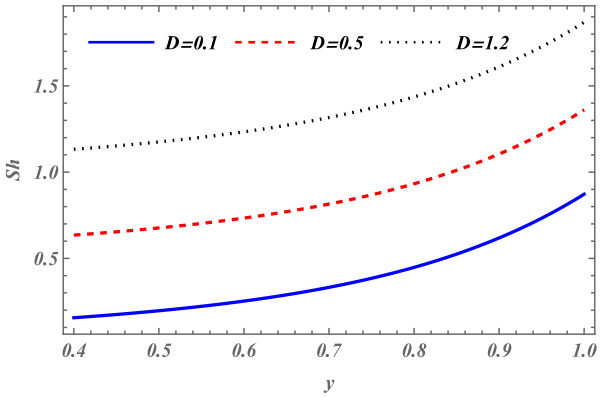

(d) Variable *D* for

$sin\alpha = 0.2, Fr = 0.2, Da = 0.5, M = 1, \mu = 0.5, \varepsilon = 0.5, \varepsilon_1 = 0.6$, β=0.4, a=1, a_1=0.4, m=2, Rd=1, Q=1, k=0.5, Sr=0.5, Sc=0.5, ζ=0.5

Fig. 20. Sherwood numbers for different parameters

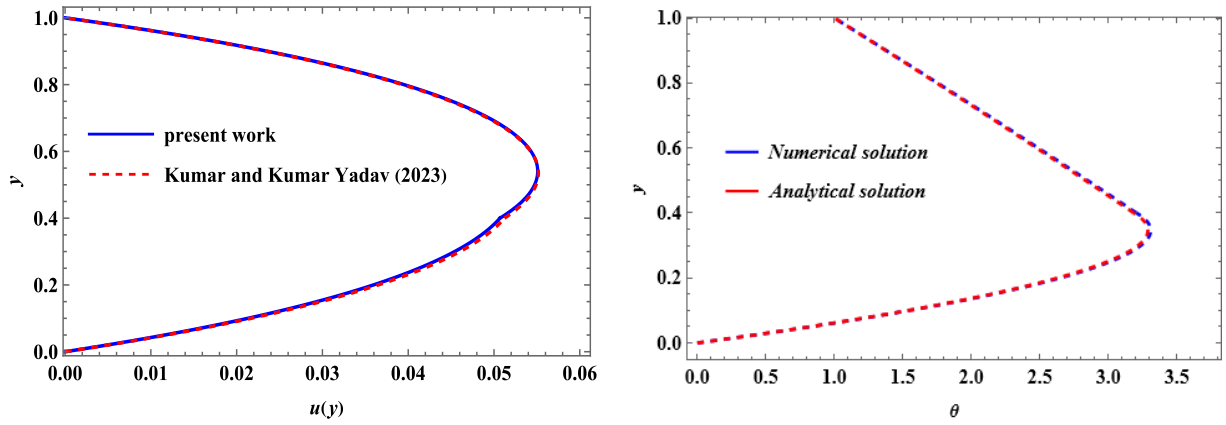

(c) Velocity profiles for

$Da = 0.5, m = 2, M = 1, sin\alpha = 0, Rd = 1,$
$\mu = 0.5, Q$=1, k=0.5, a=1, a$_1$=0.4

(d) Temprature profiles for

$Da = 0.5, m = 2, M = 1, sin\alpha = 0, Rd = 1,$
$\mu = 0.5, Q$=1, k=0.5, a=1, a$_1$=0.4

Fig. 21. Comparative study

For the Casson micropolar fluid, the Sherwood number diminishes as Sc, Sr, and ξ intensify, while for Newtonian fluid, it exhibits the opposite response, as shown in Figures 20(a), 20(b), and 20(c). Figure 20(d) reveals that as D intensifies, the Sherwood number shows a corresponding upward shift in both regions. The work from [27] can be derived from the current study by setting $\sin\alpha = 0, \beta = 0, \beta_2 = 0, \beta_1 = 0$, and $n_1 = 0$.

Figure 21(a) presents a comparison to validate the findings, while Figure 21(b) displays a comparative study of the temperature distribution between the analytical and numerical results, obtained using the fourth-order Runge–Kutta method combined with the shooting technique. One can observe that the results are in good agreement.

5. Conclusions

The investigation deals with the combined effects of velocity slip, Hall and ion slip on the heat and mass characteristics of MHD two liquid peristaltic motion through an inclined channel with a porous medium. The core and peripheral regions are respectively filled with Casson-micropolar and Newtonian liquids. The governing flow equations have been linearised under the assumption of long-wavelength approximation and small Reynolds number. The impact of pertinent parameters on resultant equations has been graphically presented and discussed. The main conclusions from the investigation are:

- Raising the porous parameter, inclination parameter, and velocity slip increases the liquid's velocity and temperature. In contrast, an increase in the magnetic field strength and Froude number reduces velocity and temperature.
- A higher diffusivity ratio enhances the concentration distribution, while the rise in the chemical reaction rate, Schmidt, and Soret numbers leads to a decline in the concentration distribution.
- The pressure gradient per wavelength grows with the rise in microrotation, magnetic field strength, micropolar fluid, Casson fluid parameter and inclination. Further, the pressure gradient reduces as the Froude number increase.
- As the values of the coupling number, Hartmann number, Casson fluid parameter, and micropolar fluid grow, the pressure rise per wavelength also rises. On the other hand, when the Froude number increase, the pressure rise per wavelength reduces.
- As the coupling, Froude, and Hartmann parameters escalate, mechanical efficiency improves, whereas inclination and Casson parameter parameters reduce it.
- The increase in the Hartmann number, the inclination parameter, and the Brinkman number contribute to a rise in the entropy generation. Enhancing the microrotation parameter drops the entropy generation.
- A rise in the inclination parameter causes the Bejan number to fall, whereas the microrotation parameter causes it to rise.
- The heat transfer rate shows an upward trend with the rise in the Hartmann number, while it declines with the Brinkman number and heat generation parameter.

- In the core region, the Sherwood number is reduced with a rise in Schmidt number, Soret number, or first-order chemical reaction rate, while a higher diffusivity ratio elevates the Sherwood number in both regions.
- The hydrodynamic situation may be established by assigning $M=0$, for the corresponding problem. Moreover, one can obtain a non-porous case by $Da\to\infty$. Furthermore, in the absence of inclination, Hall and Ion slip, velocity slip parameter, and Casson fluid (i.e. $\beta\to\infty$) parameters the results of this study correspond to those obtained by [27].

Funding Statement

This research did not receive any specific grant from funding agencies in the public, commercial, or not-for-profit sectors.

Conflicts of Interest

The author declares that there is no conflict of interest regarding the publication of this article.

Authors Contribution Statement

Surippedi Srinivas: Formal Analysis; Methodology; Supervision; Validation; Writing – Review & Editing, *J. Bala Anasuya*: Investigation; Methodology; Software; Roles/Writing – Original Draft; etc.

Appendixes

$$a_1=\frac{\sqrt{-N_5-\frac{\sqrt{-8+N_3{N_5}^2}}{\sqrt{N_3}}}}{\sqrt{2}},\ a_2=\frac{\sqrt{-N_5+\frac{\sqrt{-8+N_3{N_5}^2}}{\sqrt{N_3}}}}{\sqrt{2}}$$

$$c_5=\frac{-H+M_2-a_3^3c_6\beta_2\cosh(a_3h)+a_3^2c_6\sinh(a_3h)}{a_3^2\left(-\cosh(a_3h)+a_3\beta_2\sinh(a_3h)\right)},\ c_4=\frac{N_{21}+N_{22}+N_{23}-N_{24}}{N_{20}},$$

$$c_3=\frac{a_2N_9N_{26}\cosh[a_2h_1]+\cosh(a_3h)\left(N_{29}-N_{25}\cosh(a_1h_1)\right)+\cosh[a_1h_1]N_{28}}{N_{20}},\ c_2=\frac{-M_1N_{10}N_{34}\cosh(a_3h_1)+a_3\beta_2\sinh(a_3h)N_{35}+\cos(a_3h)N_{36}}{N_{20}}$$

$$c_1=\frac{a_2N_9N_{36}\cosh(a_2h_1)+\cosh[a_1h_1]\left(N_{39}+\cosh(a_3h)N_{43}\right)}{N_{20}}$$

$$N_{20}=\begin{pmatrix}a_3^2M_1\left(a_1N_{10}-a_2N_9\right)\begin{pmatrix}-\cosh(a_3h)\\+a_3\beta_2\sinh(a_3h)\end{pmatrix}\\\begin{pmatrix}-N_9\cosh(a_2h_1)\sinh(a_1h_1)\\+N_{10}\cosh(a_1h_1)\sinh(a_2h_1)\end{pmatrix}\end{pmatrix},$$

$$N_{21}=M_1N_9\cosh(a_3h_1)\left(H-M_2-a_3^2c_6\sinh(a_3h)\right)\begin{pmatrix}a_1\sinh(a_1h_1)\\-a_2\sinh(a_2h_1)\end{pmatrix}+a_3\beta_2\sinh(a_3h)(-a_1N_9\sinh(a_1h_1)$$

$$\left(M_1\left(-H+M_2\right)+a_3^2\left(H-M_1N_6\right)+a_3^2c_6M_1\sinh(a_3h_1)\right)+a_3^2\left(H-M_1N_6\right)\left(a_1N_{10}-a_2N_9\right)\sinh(a_2h_1)\cosh(a_1h_1)$$

$$N_{22}=a_2N_9\begin{pmatrix}M_1\left(-H+M_2\right)\sinh(a_2h_1)+a_3^2\left(H-M_1N_6\right)\sinh(a_2h_1)\\+a_3^2c_6M_1\sinh(a_2h_1)\sinh(a_3h_1)\end{pmatrix},\ N_{23}=\cosh(a_3h)(a_1N_9\sinh(a_1h_1)\begin{pmatrix}a_3^2H-HM_1+M_1M_2-a_3^2M_1N_6\\+a_3^3c_6M_1\beta_2\cosh(a_3h_1)\\+a_3^2c_6M_1\sinh(a_3h_1)\end{pmatrix}$$

$$N_{24}=\sinh(a_2h_1)(a_3^2\left(H-M_1N_6\right)\left(a_1N_{10}-a_2N_9\right)\cosh(a_1h_1)+a_2N_9\begin{pmatrix}a_3^2H-HM_1+M_1M_2-a_3^2M_1N_6\\+a_3^3c_6M_1\beta_2\cosh(a_3h_1)+a_3^2c_6M_1\sinh(a_3h_1)\end{pmatrix}$$

$$N_{26}=M_1\cosh(a_3h_1)\left(H-M_2-a_3^2c_6\sinh(a_3h)\right)-a_3\beta_2\sinh(a_3h)\begin{pmatrix}M_1\left(-H+M_2\right)+a_3^2\left(H-M_1N_6\right)\\+a_3^2c_6M_1\sinh(a_3h_1)\end{pmatrix}$$

$$N_{25}=-a_3^2\left(H-M_1N_6\right)\left(a_1N_{10}-a_2N_9\right)\cosh(a_2h_1)+a_1N_{10}\left(a_3^2H-HM_1+M_1M_2\right)$$
$$-a_1N_{10}a_3^2M_1N_6+a_1N_{10}a_3^3c_6M_1\beta_2\cosh(a_3h_1)+a_1N_{10}a_3^2c_6M_1\sinh(a_3h_1)$$

$$N_{27}=-a_3^2\left(H-M_1N_6\right)\left(a_1N_{10}-a_2N_9\right)\cosh(a_2h_1)+a_1N_{10}\left(M_1\left(-H+M_2\right)+a_3^2\left(H-M_1N_6\right)+a_3^2c_6M_1\sinh(a_3h_1)\right)$$

$$N_{28}=-a_1M_1N_{10}\cosh(a_3h_1)\left(H-M_2-a_3^2c_6\sinh(a_3h)\right)+a_3\beta_2\sinh(a_3h)N_{27}$$

$$N_{29} = a_2 N_9 \cosh(a_2 h_1)\begin{pmatrix} a_3^2 H - HM_1 + M_1 M_2 - a_3^2 M_1 N_6 + \\ a_3^3 c_6 M_1 \beta_2 \cosh(a_3 h_1) + a_3^2 c_6 M_1 \sinh(a_3 h_1) \end{pmatrix}$$

$$N_{30} = -a_3^2 (H - M_1 N_6)(a_1 N_{10} - a_2 N_9)\cosh(a_2 h_1) + a_1 N_{10}\begin{pmatrix} a_3^2 H - HM_1 + M_1 M_2 - a_3^2 M_1 N_6 + \\ a_3^3 c_6 M_1 \beta_2 \cosh(a_3 h_1) + a_3^2 c_6 M_1 \sinh(a_3 h_1) \end{pmatrix}$$

$$N_{31} = a_2 N_{10} \sinh[a_2 h_1]\begin{pmatrix} a_3^2 H - HM_1 + M_1 M_2 - a_3^2 M_1 N_6 \\ +a_3^3 c_6 M_1 \beta_2 \cosh[a_3 h_1] + a_3^2 c_6 M_1 \sinh(a_3 h_1) \end{pmatrix},\ N_{32} = \begin{pmatrix} -a_3^2 (H - M_1 N_6)(a_1 N_{10} - a_2 N_9)\cosh(a_2 h_1) \\ +a_1 N_{10}\left(M_1(-H + M_2) + a_3^2 (H - M_1 N_6) + a_3^2 c_6 M_1 \sinh(a_3 h_1)\right) \end{pmatrix}$$

$$N_{33} = -a_2 N_{10} \sinh[a_2 h_1]\left(M_1(-H + M_2) + a_3^2 (H - M_1 N_6) + a_3^2 c_6 M_1 \sinh[a_3 h_1]\right),\ N_{34} = \left(H - M_2 - a_3^2 c_6 \sinh(a_3 h)\right)\left(a_1 \sinh(a_1 h_1) - a_2 \sinh[a_2 h_1]\right)$$

$$N_{35} = \left(N_{33} + N_{32} \sinh(a_1 h_1)\right),\ N_{36} = \left(N_{31} - N_{30} \sinh[a_1 h_1]\right),\ N_{36} = \begin{pmatrix} M_1 \cosh(a_3 h_1)\left(-H + M_2 + a_3^2 c_6 \sinh(a_3 h)\right) \\ +a_3 \beta_2 \sinh(a_3 h)\begin{pmatrix} M_1(-H + M_2) + a_3^2 (H - M_1 N_6) \\ +a_3^2 c_6 M_1 \sinh(a_3 h_1) \end{pmatrix} \end{pmatrix}$$

$$N_{37} = a_1 M_1 N_{10} \cosh(a_3 h_1)\left(H - M_2 - a_3^2 c_6 \sinh(a_3 h)\right),\ N_{38} = \begin{pmatrix} a_3^2 (H - M_1 N_6)(a_1 N_{10} - a_2 N_9)\cosh(a_2 h_1) \\ -a_1 N_{10}\begin{pmatrix} M_1(-H + M_2) + a_3^2 (H - M_1 N_6) \\ +a_3^2 c_6 M_1 \sinh(a_3 h_1) \end{pmatrix} \end{pmatrix}$$

$$N_{39} = \left(N_{37} + a_3 \beta_2 N_{38} \sinh(a_3 h)\right),\ N_{40} = \begin{pmatrix} a_3^2 H - HM_1 + M_1 M_2 - a_3^2 M_1 N_6 \\ +a_3^3 c_6 M_1 \beta_2 \cosh(a_3 h_1) + a_3^2 c_6 M_1 \sinh(a_3 h_1) \end{pmatrix}$$

$$N_{41} = \left(-a_3^2 (H - M_1 N_6)(a_1 N_{10} - a_2 N_9)\cosh(a_2 h_1) + a_1 N_{10} N_{42}\right),\ N_{42} = \begin{pmatrix} a_3^2 H - HM_1 + M_1 M_2 - a_3^2 M_1 N_6 \\ +a_3^3 c_6 M_1 \beta_2 \cosh(a_3 h_1) + a_3^2 c_6 M_1 \sinh(a_3 h_1) \end{pmatrix}$$

$$N_{43} = \left(-a_2 N_9 \cosh(a_2 h_1) N_{40} + \cosh(a_1 h_1) N_{41}\right)$$

$$A_{14} = -a_3 Brc_5^2 + a_3 Brc_6^2 + a_3^3 Brc_5^2 J - a_3^3 Brc_6^2 J + 2a_3 J \Upsilon_1 + 2a_3 BrG_3^2$$

$$A_{15} = \frac{Br\left(c_5^2 + c_6^2\right)\left(1 + a_3^2 J\right)}{2a_3},\ A_{16} = \frac{Brc_5 c_6}{a_3}, A_{17} = a_3 Brc_5 c_6 J,$$

$$A_{18} = \frac{8Brc_6 G_3}{a_3}, A_{19} = \frac{8Brc_5 G_3}{a_3}$$

$$A_1 = 2Brc_3^2 N_{10}^2 - 2a_2^2 Brc_3^2 N_{10}^2 - 2Brc_4^2 N_{10}^2 + 2a_2^2 Brc_4^2 N_{10}^2 + 2Brc_1^2 N_9^2 - 2a_1^2 Brc_1^2 N_9^2$$
$$- 2Brc_2^2 N_9^2 + 2a_1^2 Brc_2^2 N_9^2 + 4\Upsilon_1 + 4BrG_2^2$$

$$A_2 = \frac{\left(1 + a_1^2\right) Br\left(c_1^2 + c_2^2\right) N_9^2}{a1^2},\ A_3 = \frac{8Brc_1 c_3 N_{10} N_9}{\left(a_1 - a_2\right)^2} - \frac{8a_1 a_2 Brc_1 c_3 N_{10} N_9}{\left(a_1 - a_2\right)^2} - \frac{8Brc_2 c_4 N_{10} N_9}{\left(a_1 - a_2\right)^2} + \frac{8a_1 a_2 Brc_2 c_4 N_{10} N_9}{\left(a_1 - a_2\right)^2}$$

$$A_4 = Brc_3^2 N_{10}^2 + \frac{Brc_3^2 N_{10}^2}{a_2^2} + Brc_4^2 N_{10}^2 + \frac{Brc_4^2 N_{10}^2}{a_2^2},$$

$$A_5 = \frac{8Brc_1 c_3 N_{10} N_9}{\left(a_1 + a_2\right)^2} + \frac{8a_1 a_2 Brc_1 c_3 N_{10} N_9}{\left(a_1 + a_2\right)^2} + \frac{8Brc_2 c_4 N_{10} N_9}{\left(a_1 + a_2\right)^2} + \frac{8a_1 a_2 Brc_2 c_4 N_{10} N_9}{\left(a_1 + a_2\right)^2},$$

$$A_6 = 2Brc_1 c_2 N_9^2 + \frac{2Brc_1 c_2 N_9^2}{a_1^2},\ A_7 = \frac{8Brc_2 c_3 N_{10} N_9}{\left(a_1 - a_2\right)^2} - \frac{8a_1 a_2 Brc_2 c_3 N_{10} N_9}{\left(a_1 - a_2\right)^2} - \frac{8Brc_1 c_4 N_{10} N_9}{\left(a_1 - a_2\right)^2} + \frac{8a_1 a_2 Brc_1 c_4 N_{10} N_9}{\left(a_1 - a_2\right)^2}$$

$$A_8 = 2Brc_3 c_4 N_{10}^2 + \frac{2Brc_3 c_4 N_{10}^2}{a_2^2},$$

$$A_9 = \frac{8Brc_2 c_3 N_{10} N_9}{\left(a_1 + a_2\right)^2} + \frac{8a_1 a_2 Brc_2 c_3 N_{10} N_9}{\left(a_1 + a_2\right)^2} + \frac{8Brc_1 c_4 N_{10} N_9}{\left(a_1 + a_2\right)^2} + \frac{8a_1 a_2 Brc_1 c_4 N_{10} N_9}{\left(a_1 + a_2\right)^2}$$

$$A_{10}=\frac{16Brc_1N_9G_2}{a_1^{\,2}},A_{11}=\frac{16Brc_3N_{10}G_2}{a_2^{\,2}},A_{12}=\frac{16Brc_2N_9G_2}{a_1^{\,2}},A_{13}=\frac{16Brc_4N_{10}G_2}{a_2^{\,2}}$$

$$d_1=\frac{A_2+A_3+A_4+A_5+A_{10}+A_{11}}{8\left(1+Rd\right)},\quad A_{20}=\frac{2SryA_1}{f_1^2},A_{21}=\frac{2a1SrA_2}{4a1^2-f_1^2},\quad A_{22}=\frac{-a_1SrA_3+a_2SrA_3}{\left(a_1-a_2-f_1\right)\left(a_1-a_2+f_1\right)},A_{23}=\frac{2a_2SrA_4}{4a_2^{\,2}-f_1^2},$$

$$f_3=\frac{1}{8a_3J\left(1+Rd\right)\left(h+h_1\left(-1+\kappa\right)\right)},8a_3J\kappa f_3+8f_3a_3JRd\,\kappa+f_3a_3h_1J\left(2h+h_1\left(-2+\kappa\right)\right)A_1-a_3f_3J\kappa A_3$$

$$+2f_3a_3J\sinh\left(a_1h_1\right)\left(2a_1\left(h-h_1\right)\cosh\left(a_1h_1\right)+\kappa f_3\sinh\left(a_1h_1\right)\right)A_2+a_3f_3J\kappa\cosh\left(\left(a_1-a_2\right)h_1\right)A_3+f_3a_1a_3hJ\sinh\left(\left(a_1-a_2\right)h_1\right)A_3$$

$$-f_3a_2a_3hJ\sinh\left(\left(a_1-a_2\right)h_1\right)A_3-f_3a_1a_3h_1J\sinh\left(\left(a_1-a_2\right)h_1\right)A_3+a_2a_3h_1f_3J\sinh\left(\left(a_1-a_2\right)h_1\right)A_3-a_3Jf_3\kappa A_4+a_3Jf_3\kappa\cosh\left(2a_2h_1\right)A_4$$

$$+2f_3a_2a_3hJ\sinh\left(2a_2h_1\right)A_4-2f_3a_2a_3h_1J\sinh\left(2a_2h_1\right)A_4-a_3f_3J\kappa A_5+a_3f_3J\kappa\cosh\left(\left(a_1+a_2\right)h_1\right)A_5+a_1f_3a_3hJ\sinh\left(\left(a_1+a_2\right)h_1\right)A_5$$

$$+a_2f_3a_3hJ\sinh\left(\left(a_1+a_2\right)h_1\right)A_5-a_1f_3a_3h_1J\sinh\left(\left(a_1+a_2\right)h_1\right)A_5-a_2a_3h_1Jf_3\sinh\left[\left(a_1+a_2\right)h_1\right]A_5+2f_3a_1a_3hJ\cosh\left(2a_1h_1\right)A_6$$

$$-2f_3a_1a_3h_1J\cosh\left(2a_1h_1\right)A_6+a_3f_3J\kappa\sinh\left(2a_1h_1\right)A_6+a_1a_3hf_3J\cosh\left(\left(a_1-a_2\right)h_1\right)A_7-a_2a_3hJf_3\cosh\left(\left(a_1-a_2\right)h_1\right)A_7$$

$$-a_1a_3h_1Jf_3\cosh\left(\left(a_1-a_2\right)h_1\right)A_7+a_2a_3h_1Jf_3\cosh\left(\left(a_1-a_2\right)h_1\right)A_7+a_3J\kappa f_3\sinh\left(\left(a_1-a_2\right)h_1\right)A_7+2f_3a_2a_3hJ\cosh\left(2a_2h_1\right)A_8$$

$$-2a_2a_3h_1Jf_3\cosh\left(2a_2h_1\right)A_8+a_3J\kappa f_3\sinh\left(2a_2h_1\right)A_8+a_1a_3hJf_3\cosh\left(\left(a_1+a_2\right)h_1\right)A_9+a_2a_3hJf_3\cosh\left(\left(a_1+a_2\right)h_1\right)A_9$$

$$-a_1a_3h_1Jf_3\cosh\left(\left(a_1+a_2\right)h_1\right)A_9-a_2a_3h_1f_3J\cosh\left(\left(a_1+a_2\right)h_1\right)A_9$$

$$A_{24}=\frac{-a_1SrA_5-a_2SrA_5}{\left(a_1+a_2\right)^2-f_1^2},A_{25}=\frac{2a_1SrA_6}{4a_1^{\,2}-f_1^{\,2}},\quad A_{26}=\frac{-a_1SrA_7+a_2SrA_7}{\left(a_1-a_2\right)^2-f_1^2},\quad A_{29}=\frac{a_1SrA_{10}}{a_1^{\,2}-f_1^{\,2}},\quad A_{27}=\frac{2a_2SrA_8}{4a_2^{\,2}-f_1^{\,2}}\quad A_{28}=\frac{-a_1SrA_9-a_2SrA_9}{\left(a_1+a_2\right)^2-f_1^2}$$

$$A_{30}=\frac{a_2SrA_{11}}{a_2^{\,2}-f_1^{\,2}},A_{31}=\frac{a_1SrA_{12}}{a_1^{\,2}-f_1^{\,2}},\quad A_{32}=\frac{a_2SrA_{13}}{a_2^{\,2}-f_1^{\,2}},A_{33}=\frac{d_2Sr}{f_1^{\,2}},\quad A_{34}=\frac{Sr\mu A_{14}}{2a_3J\left(1+Rd\right)f_2^{\,2}},\quad A_{35}=\frac{Sr\mu A_{15}}{2J\left(1+Rd\right)\left(-4a_3^{\,2}+f_2^{\,2}\right)},$$

$$A_{38}=\frac{Sr\mu A_{18}}{4J\left(1+Rd\right)\left(-a_3^{\,2}+f_2^{\,2}\right)},\quad A_{36}=\frac{Sr\mu A_{16}}{2J\left(1+Rd\right)\left(-4a3^2+f_2^{\,2}\right)}+\frac{Sr\mu A_{17}}{2J\left(1+Rd\right)\left(-4a3^2+f_2^{\,2}\right)},$$

$$A_{39}=\frac{Sr\mu A_{19}}{4J\left(1+Rd\right)\left(-a_3^{\,2}+f_2^{\,2}\right)},\quad A_{40}=\frac{d_4Sr}{f_2^{\,2}}$$

References

[1] Latham, T.W., 1966. Fluid motions in a peristaltic pump., Ph.D. thesis, Massachusetts Institute of Technology.

[2] Shapiro, A.H., Jaffrin, M.Y., and Weinberg, S. L., 1969. Peristaltic pumping with long wavelengths at low reynolds number. *Journal of fluid mechanics*, 37(4), pp. 799–825

[3] Srivastava, L, Srivastava, V., and Sinha, S., 1983. Peristaltic transport of a physiological fluid. *Biorheology*, 20(2), pp. 153–166.

[4] Hayat, T., Wang, Y., Siddiqui, A., Hutter, K., and Asghar, S., 2002. Peristaltic transport of a third-order fluid in a circular cylindrical tube. *Mathematical Models and Methods in Applied Sciences*, 12 (12), pp. 1691–1706.

[5] Mishra, M., and Ramachandra Rao, A., 2003. Peristaltic transport of a newtonian fluid in an asymmetric channel. *Zeitschrift für angewandte Mathematik und Physik ZAMP*, 54, pp. 532–55

[6] Radhakrishnamacharya, G., and Srinivasulu, C., 2007. Influence of wall properties on peristaltic transport with heat transfer. *Comptes Rendus Mecanique*, 335(7), 36.

[7] Srinivas, S., and Kothandapani, M., 2008. Peristaltic transport in an asymmetric channel with heat transfer—a note. *International Communications in Heat and Mass Transfer*, 35 (4), pp. 514–522.

[8] Pandey, S., and Chaube, M.K., 2010. Peristaltic transport of a visco-elastic fluid in a tube of non-uniform cross section. *Mathematical and Computer Modelling*, 52(3-4), pp. 501–514.

[9] Srinivas, S., and Muthuraj, R., 2010. Peristaltic transport of a jeffrey fluid under the effect of slip in an inclined asymmetric channel. *International Journal of Applied Mechanics*, 2(02), pp. 437–455.

[10] Srinivas, S., and Muthuraj, R., 2011. Effects of chemical reaction and space porosity on mhd mixed convective flow in a vertical asymmetric channel with peristalsis. *Mathematical and Computer Modelling*, 54(5-6), pp. 1213–1227.

[11] Magesh, A., Pushparaj, V., Srinivas, S., and Tamizharasi, P., 2023. Numerical investigations of activation energy on the peristaltic transport of carreau nanofluid through a curved asymmetric channel. *Physics of Fluids*, 35(10).

[12] Abbasi, A., Danish, S., Farooq, W., Khan, M.I., Akermi, M., and Hejazi, H.A., 2024. Peristaltic transport of viscoelastic fluid in curved ducts with ciliated walls. *Physics of Fluids*, 36(3).

[13] Anasuya, J.B., and Srinivas, S., 2024. Pulsatile flow and peristaltic motion interaction of Walter's B liquid. Proceedings of the Institution of Mechanical Engineers. *Part E: Journal of Process Mechanical Engineering*, 2024 Apr 12:09544089241242601.

[14] Das, S., Barman, B., Jana, R.N., and Makinde, O.D., 2021. Hall and ion slip currents' impact on electromagnetic blood flow conveying hybrid nanoparticles through an endoscope with peristaltic waves. *BioNanoScience*, 11(3), pp. 770-792.

[15] Das, S., and Barman, B., 2022. Ramification of hall and ion-slip currents on electro-osmosis of ionic hybrid nanofluid in a peristaltic microchannel. *BioNanoScience*, 12(3), pp. 957-978.

[16] Srinivas, S., Anasuya, J.B., and Merugu, V., 2025. Interaction of pulsatile and peristaltic flow of a particle-fluid suspension with thermal effects. *International Communications in Heat and Mass Transfer*, 163, 108728.

[17] Shukla, J.B., Parihar, R.S., Rao, B.R.P., and Gupta, S.P., 1980. Effects of peripheral-layer viscosity on peristaltic transport of a bio-fluid. *Journal of Fluid Mechanics*, 97(2), pp. 225–237.

[18] Srivastava, V., and Saxena, M., 1995. A two-fluid model of non-newtonian blood flow induced by peristaltic waves. *Rheologica Acta*, 34, pp. 406–414.

[19] Rao, A. R., and Usha, S., 1995. Peristaltic transport of two immiscible viscous fluids in a circular tube. *Journal of Fluid Mechanics*, 298, pp. 271–285.

[20] Misra, J., and Pandey, S., 2001. Peristaltic flow of a multilayered power-law fluid through a cylindrical tube. *International Journal of Engineering Science*, 39(4), pp. 387–402.

[21] Kavitha, A., Reddy, R.H., Saravana, R., and Sreenadh, S., 2017. Peristaltic transport of a jeffrey fluid in contact with a newtonian fluid in an inclined channel. *Ain Shams Engineering Journal*, 8(4) pp. 683–687.

[22] Vajravelu, K., Sreenadh, S., and Saravana, R., 2017. Influence of velocity slip and temperature jump conditions on the peristaltic flow of a jeffrey fluid in contact with a newtonian fluid. *Applied Mathematics and Nonlinear Sciences*, 2 (2), pp. 429–442.

[23] Hussain, S., Ali, N., and Ullah, K., 2019. Peristaltic flow of phan-thien-tanner fluid: effects of peripheral layer and electro-osmotic force. *Rheologica Acta*, 58, pp. 603–618.

[24] Ali, N., Hussain, S., Ullah, K., and Bég, O.A., 2019. Mathematical modelling of two-fluid electroosmotic peristaltic pumping of an ellis fluid in an axisymmetric tube. *The European Physical Journal Plus*, 134(4), 141.

[25] Sankranthi, V.K., and Akkiraju Naga Satya, S., 2021. Influence of peristalsis on the convective flow of two immiscible fluids in a vertical channel. *Heat Transfer*, 50(5), pp. 4757–4774.

[26] Rushi Kesava, A., and Srinivas, A., 2022. Exploration of peristaltic pumping of casson fluid flow through a porous peripheral layer in a channel. *Nonlinear Engineering*, 11(1), pp. 558– 567.

[27] Sreenadh, S., Arunachalam, P., Sumalatha, B., 2021. Peristaltic flow of two-layered fluids in an elastic tube. *Proceedings of the National Academy of Sciences, India Section A: Physical Sciences*, pp. 1–12.

[28] Kumar, A., and Yadav, P.K., 2023. Heat and mass transfer in peristaltic flow of mhd non-miscible micropolar and newtonian fluid through a porous saturated asymmetric channel. *Waves in Random and Complex Media*, pp. 1–45.

[29] Jubair, S., Yang, J., Ali, B., Bin-Mohsin, B., and Abd El-Wahed Khalifa, H., 2025. Analyzing the impact of non-Newtonian nanofluid

flow on pollutant discharge concentration in wastewater management using an artificial computing approach. *Applied Water Science*, 15, pp. 1-13.

[30] Jubair, S., Ali, B., Rafique, K., Ahmad Ansari, M., Mahmood, Z., Kumar, A., Mukalazi, H., and Alqahtani, H., 2024. Couple-stress nanofluid flow comprised of titanium alloy subject to Hall current and Joule heating effects: Numerical investigation. *AIP Advances*, 14(11), 115101.

[31] Mehmood, Z., Mehmood, R., and Iqbal Z., 2017. Numerical investigation of micropolar casson fluid over a stretching sheet with internal heating. *Communications in Theoretical Physics*, 67(4), 443.

[32] Iqbal, Z., Mehmood, R., and Azhar, E., Mehmood, Z., 2017. Impact of inclined magnetic field on micropolar casson fluid using keller box algorithm. *The European Physical Journal Plus*, 132, pp. 1–13.

[33] Chun, O., Raja, M.A.Z., Naz, S., Ahmad, I., Akhtar, R., Ali, Y., and Shoaib, M., 2020. Dynamics of inclined magnetic field effects on micropolar casson fluid with lobatto iiia numerical solver. *AIP Advances*, 10(6).

[34] Hazarika, S., and Ahmed, S., 2020. Steady magnetohydrodynamic micropolar casson fluid of brownian motion over a solid sphere with thermophoretic and buoyancy forces: numerical analysis. *Journal of Nanofluids*, 9(4), pp. 336–345.

[35] El-Dabe, N.T., Moatimid, G.M., Elshekhipy, A.-E. A., and Aballah, N.F., 2020. Numerical simulation of the motion of a micropolar casson fluid through a porous medium over a stretching surface. *Thermal Science*, 24(2 Part B), pp. 1285–1297.

[36] Abbas, Z., and Rafiq, M., 2022. Numerical simulation of thermal transportation with viscous dissipation for a peristaltic mechanism of micropolar-casson fluid. *Arabian Journal for Science and Engineering*, 47(7), pp. 8709–8720.

[37] Upadhya, S.M., Raju, S.V.S.R., Raju, C.S.K., Shah, N.A., and Chung, J.D., 2022. Importance of entropy generation on casson, micropolar and hybrid magneto-nanofluids in a suspension of cross diffusion. *Chinese Journal of Physics*, 77, pp. 1080–1101.

[38] Abbas, N., Shatanawi, W., and Shatnawi, T.A. 2024. Thermodynamic properties of casson-sutterbymicropolar fluid flow over exponential stretching curved sheet with impact of mhd and heat generation. *Case Studies in Thermal Engineering*, 55, 104123.

[39] Sharma, V., Chandrawat, R.K., and Kumar D., 2024. Numerical investigation of unsteady mhd immiscible casson micropolar and jeffery fluid in a horizontal channel with heat transfer using mcb-dqm approach. *Numerical Heat Transfer, Part B: Fundamentals*, pp. 1–35.

[40] Vaidehi, P., and Sasikumar, J., 2024. Significance of micro-rotation on buoyancy driven oscillatory flow of micropolar-casson fluid through tapered wavy channels: A numerical approach. *International Journal of Applied and Computational Mathematics*, 10(3) pp. 1–26.

[41] Imran, N., Javed, M., Sohail, M., Thounthong, P., Nabwey, H.A., and Tlili, I., 2020. Utilization of hall current and ions slip effects for the dynamic simulation of peristalsis in a compliant channel. *Alexandria Engineering Journal*, 59(5), pp. 3609-3622.

[42] Das, S., Barman, and Jana, R., 2021. Hall and ion-slip currents' role in transportation dynamics of ionic Casson hybrid nano-liquid in a microchannel via electroosmosis and peristalsis. *Korea-Australia Rheology Journal*, 33, pp. 367-391.

[43] Krishna, M.V., and Chamkha, A.J., 2019. Hall and ion slip effects on MHD rotating boundary layer flow of nanofluid past an infinite vertical plate embedded in a porous medium. *Results in Physics*, 15. 102652.

[44] Das, S., Barman, B., and Jana R., 2021. Influence of hall and ion-slip currents on peristaltic transport of magneto-nanofluid in an asymmetric channel. *BioNanoScience*, 11, pp. 720–738

[45] Bejan, A., 1996. Entropy generation minimization: The new thermodynamics of finite-size devices and finite-time processes. *Journal of Applied Physics*, 79(3), pp. 1191–1218.